Data-driven control of a Pendulum Wave Energy Converter: A Gaussian Process Regression approach

Data-driven Control of a Pendulum Wave Energy Converter: a Gaussian Process Regression approach

Daniele Giovanni Gioia[a], Edoardo Pasta[b,*], Paolo Brandimarte[a] and Giuliana Mattiazzo[b]

[a]Department of Mathematical Sciences "Giuseppe Luigi Lagrange", DISMA, Politecnico di Torino, 10129, Corso Duca degli Abruzzi 24, Turin (TO), Italy.

[b]Marine Offshore Renewable Energy Lab (MOREnergyLab), DIMEAS, Politecnico di Torino, 10129, Corso Duca degli Abruzzi 24, Turin (TO), Italy.

ARTICLE INFO

Keywords:
Wave Energy
Pendulum Wave Energy Converter
Data-driven Control
CoKriging
Gaussian Process Regression

ABSTRACT

The energy coming from the motion of the waves of seas and oceans could be an important component in the solution of the energy problem related to the pursuit of alternatives to fossil fuels. However, wave energy is still technologically immature and it has not reached the economic feasibility required for economy of scale. One of the major technological challenges for the achievement of this goal is the development of control strategies capable of maximizing the extracted energy, adapting to the conditions of the seas and oceans that surround the Wave Energy Converter (WEC) devices. To perform this task, control systems often adopt explicitly control-oriented models, that are by nature affected by uncertainties. On the contrary, to address the problem a data-driven solution is proposed here. The presented strategy applies an optimization approach based on a Gaussian Process Regression (GPR) metamodel to learn the control strategy to be applied. In order to accelerate the learning process, we present a novel method that exploits in the initial phase a previous knowledge given by simulations with the system model and based on the co-kriging concept. To test this approach the Pendulum Wave Energy Converter has been adopted as a case study. To differentiate the previous knowledge and the real system behaviour, a simplified linear model is used to obtain the prior knowledge, while a complex nonlinear one acts as the environment in which simulate the behaviour of the real system. A month-long simulation is used to validate the effectiveness of the proposed strategy, showing the ability of adapting to a real system different from the simplified model on the basis only of data, and overcoming the model-based strategy in terms of performance.

1. Introduction

In the present context, characterized by a growing awareness for issues such as global warming, energy exploitation, and rising CO2 levels, a remarkable amount of research is directed towards new approaches for electricity generation from different renewable sources. Among the studied technologies related to renewable energy sources, wave energy is one of the most promising (Mattiazzo, 2019). Unlike other types of energy conversion technologies, such as photovoltaic plants or wind turbines, wave energy converters (WECs) have not reached a sufficient level of technological maturity, nor the proposed solutions to the problem of extracting energy from sea and oceans have managed to converge to a definitive concept and design (Guo and Ringwood, 2021), (Trueworthy and DuPont, 2020). Indeed, several challenges have to be faced in the wave energy context to effectively capture the energy coming from this type of source. Among them, one of the most crucial is the development of suitable advanced control strategies for WEC devices (Ringwood, 2020).

Suitable control systems for a WEC should be able to adapt to the different sea conditions that the device will face after being deployed, providing the optimal action able to maximize the absorbed power. Usually, the control strategies that are adopted are *model-based*. This means that the computation of the control action relies on a simplified model of the system. This type of model is usually a linearized version that neglects system nonlinearities in the system itself and possible nonlinear phenomena arising from its interaction with the environment, like nonlinear Froude-Krylov forces (Giorgi et al., 2020). To overcome possibly too strong simplifications, some novel techniques have tried to reformulate

*Corresponding author
daniele.gioia@polito.it (D.G. Gioia); edoardo.pasta@polito.it (E. Pasta); paolo.brandimarte@polito.it (P. Brandimarte); giuliana.mattiazzo@polito.it (G. Mattiazzo)
ORCID(s): 0000-0001-8979-4174 (D.G. Gioia); 0000-0001-9525-6284 (E. Pasta); 0000-0002-6533-3055 (P. Brandimarte); 0000-0002-7212-2299 (G. Mattiazzo)

more complex nonlinear models in a control-oriented form (Faedo et al., 2020). However, one of the issues related to model-based control strategies remains the need of dealing with uncertainties related to the differences between the adopted model and the real system (Ringwood et al., 2020), especially the ones associated to the formulation of the hydrodynamic contributions. Moreover, since this type of plants is supposed to work for a long period of time, it is reasonable that, because of aging phenomena like biofouling growing on the hull or eventual faults, the differences between the actual deployed system and the simplified model adopted in the control computation will increase with time. This has motivated the adoption of data-driven, model-free control approaches.

1.1. Motivation and paper positioning

Based on the reasons described above, in this paper we experiment with data-driven control design for the *Pendulum Wave Energy Converter* (PeWEC) (Pozzi et al., 2018a), (Sirigu et al., 2020) as a case study. The proposed control strategy is based on *surrogate optimization* and *Gaussian Process Regression* (GPR), which is an extension of traditional *Kriging* metamodels, (Forrester and Keane, 2009). The general idea is to learn a surrogate model (also known as a metamodel) by exploiting control experiences, directly linking control design parameters with expected performance. One of the advantages of this strategy is that it does not necessarily rely on a previously built model of the system, avoiding the related uncertainties and modelling errors. However, there are disadvantages too. On the one hand, it might be unwise to start operations on the actual system without any pre-learned control strategy, possibly based on a simplified and tentative system model, which is supposed to be available. On the other one, sea state occurrences are not uniform, and learning in some sea states might be overly slow. Then, the problem arises of merging two sources of knowledge: what we can learn from simplified simulations, and what we can learn online, from the physical system operation. To this aim, we adopt a *Multi-Fidelity* (MF) surrogate model (Forrester et al., 2007). The MF approach has a wide range of potential applications, where we want to merge multiple sources of knowledge. On the one hand, when a suitable but expensive simulation model is available, we may improve speed of learning by merging computer-based simulations relying on an simplified, but efficient, model with simulations of the more realistic, but time consuming, model. On the other one, we may merge knowledge based on a simplified simulation model with online experiments with the physical system. Indeed, the main contribution of the paper is the experimentation and validation of MF surrogate models to WEC control design. We will adopt a very simple control approach, essentially based on reactive control (Maria-Arenas et al., 2019; Ringwood et al., 2014), taking the specific sea-state occurrence into account.

Since actual experience with a physical WEC would be prohibitive, in order to validate the approach and show its potential, we will take a twin-model approach. We simulate both a simple linearized model of PeWEC and a nonlinear one, which will play the role of the model and the actual physical system in operational conditions, respectively. To add further verisimilitude to the adopted model, instead of adopting a regular wave assumption, the forces acting on the hull have been modeled as characterized by random amplitude and phase, as presented in (Merigaud and Ringwood, 2018). This framework is actually quite relevant when dealing with model-based control. Consider, for instance, the selection of weights in a Model Predictive Control (MPC) approach (Faedo et al., 2017). The simulation of an MPC strategy on a complex nonlinear system is quite expensive, and a surrogate model could become necessary for an accurate optimization. In that case too, a MF based approach may be helpful.

Hence, the reported experience aims at more general purposes within the control design for WECs. The specific WEC system and the specific control strategy that we adopt should be just regarded as a suitable testbed for the application of data-driven learning of control strategies, based on MF surrogate models.

1.2. Plan of the paper

The remainder of the paper is organized as follows. In Sect. 2 the model of PeWEC is presented in its nonlinear and linearized forms, together with the main parameters characterizing the PeWEC under study. In Sect. 3 the optimal control problem is presented, together with a brief description of the state-of-the-art of WEC control and the actual control strategy adopted in PeWEC applications. In Sect. 4 the algorithm based on GPR optimization adopted in the optimal control computation is described, while in Sect. 5 some considerations have been made to choose the proper kernel behind this type of approach. In Sec. 6 the settings adopted in the learning experience simulations are presented, together with the discussion of the obtained results. Finally in the conclusions section, some considerations are made about the proposed control strategy.

The reader will find a list of the adopted symbols in Table 2 and Table 3, regarding the Gaussian Process Regression notation and the PeWEC device respectively.

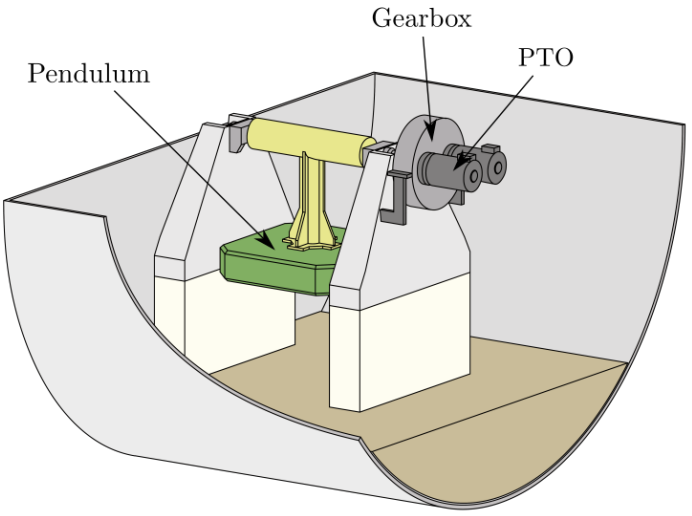

Figure 1: Graphical representation of the PeWEC device.

2. PeWEC Device

PeWEC is a pitching-resonant floating WEC, that is able, by means of a pendulum system, to extract energy from the pitching motion generated by the action that the waves exert on the hull. Other concepts of pendulum-based WECs can be found in (Alevras et al., 2015; Yurchenko and Alevras, 2018). The main components besides the pendulum and the floater are the *Power Take-Off* (PTO) and the mooring system (Pozzi et al., 2018b). The PTO and the pendulum are responsible of the conversion process, and are enclosed in the hull, making them protected against the corrosive action of the water, and guaranteeing an higher durability. More in particular, the pendulum hinge is connected directly to the shaft of the PTO itself, which is integral with the hull structure, by means of a gearbox. In this way, the oscillating motion of the pendulum due to the pitching motion of the floater is directly converted into electrical energy by means of the generator.

Assuming a properly designed mooring system, PeWEC can be considered to be self-orienting with respect to the incoming wave. In this way, its main floater motions are pitch, surge and heave. Because of that, being sway, roll and yaw negligible, they will not be considered in the formulation of the PeWEC models used in the simulations. A schematic representation of PeWEC is presented in Fig. 1. With these assumptions, the vector of the coordinates that describe the floater motion is formulated in (1),

$$X_f(t) = \left[x(t), z(t), \delta(t)\right]^\mathsf{T} \tag{1}$$

where $x(t)$ and $z(t)$ are the floater surge and heave, while $\delta(t)$ is the rotation of the floater with respect to the inertial axis y. Assuming the principles of linear wave theory valid, together with small floater oscillations, the equation that regulates the floater motion is the Cummins' one in (2),

$$\left(M + A_\infty\right)\ddot{X}_f(t) + \int_0^t K_r\left(t-\tau\right)\dot{X}_f(t)d\tau + B_v|\dot{X}_f(t)|\dot{X}_f(t) + K_h X_f(t) = F_{ext}(t) \tag{2}$$

where $\boldsymbol{M}$ is the inertia matrix that takes into account of both the hull and the internal components of PeWEC, $\boldsymbol{A_\infty}$ is the added mass at infinity frequency, $\boldsymbol{K_r}$ is the radiation impulse response functions matrix, $\boldsymbol{K_h}$ is the hydrostatic stiffness matrix, and $\boldsymbol{F_{ext}}(t)$ are the external forces acting on the different degrees of freedom of the floater. The coefficients $\boldsymbol{B_v}$ related to the nonlinear viscous forces has been computed by means of fully-viscous *Computational Fluid Dynamics* (CFD) simulations of the PeWEC structure (Fontana et al., 2020). The convolution term and the added mass contribution constitute the radiation forces. In particular, the convolution term may be approximated by a

state-space representation:

$$\int_0^t K_r\left(t-\tau\right)\dot{X}_f(t)d\tau = F_r(t) \simeq \begin{cases} \dot{\zeta}_r(t) & = A_r\zeta_r(t) + B_r\dot{X}_f(t) \\ F_r(t) & = C_r\zeta_r(t) + D_r\dot{X}_f(t) \end{cases}, \tag{3}$$

where $\zeta_r(t)$ is an array of additional states used to represent the convolution term F_r of the radiation forces acting on the hull. The system state space matrices A_r, B_r, C_r, and D_r have been computed in this work by means of the *Finite Order Approximation by Moment-Matching* (FOAMM) toolbox (Faedo et al., 2018). The external forces $F_{ext}(t)$ include contributions from the wave, the mooring, and the reactions that the pendulum and PTO system discharge onto the hull axes:

$$F_{ext}(t) = F_{wave}(t) + F_{moor}(t) + F_{pend}(t). \tag{4}$$

In (4), the first term $F_{wave}(t)$ has been computed considering the wave forces as the superposition of several sinusoidal components that follows a *JONSWAP* (Joint North Sea Wave Observation Project) wave spectrum. More in particular, considering a spectrum $S_\eta(\omega)$ of N components and component amplitudes that follows the *Random Amplitude scheme* presented in (Merigaud and Ringwood, 2018), the wave elevation can be written as:

$$\eta(t) = \sum_{n=1}^{N} A_n \sin\left(\omega_n t + \theta_n\right), \tag{5}$$

where the n-th component has frequency ω_n, amplitude A_n that follows a Rayleigh distribution with variance $2S_\eta(\omega_n)\Delta\omega$, and a random phase θ_n chosen following a uniform distribution between 0 and 2π. In this way, the wave force acting on the i-th axis of the hull $F_{wave,i}(t)$ is given by:

$$F_{wave_i}(t) = \sum_{n=1}^{N} |f_{e_{i,n}}| A_n \sin\left(\omega_n t + \theta_n + \angle f_{e_{i,n}}\right). \tag{6}$$

In (6), $f_{e_{i,n}}$ is the excitation force n-th geometry-dependent coefficient, at frequency ω_n and computed with respect to the i-th axis, by means of NEMOH Babarit and Delhommeau (2015), an open-source tool for *Boundary Element Method* (BEM) computations. It is important to notice that the presence of the random contributions in the wave force will affect the power absorbed by the PeWEC device, making its value non deterministic.

The mooring system that has been considered in this work is composed of 4 lines, each one having a contribution in the term $F_{moor}(t)$ in (4) that has been modelled following the *Quasi-static* (QS) approach presented in (Paduano et al., 2020). This has been done because of the strong influence that the mooring has on the productivity in the real systems (Niosi et al., 2021; Paduano et al., 2021).

The force terms $F_{pend}(t)$ in (6) related to the pendulum dynamics are generated by the oscillation of the pendulum itself around the hinge, as it can be seen from the scheme in Fig.2. Defined the global, the floater and the pendulum reference frames as $\mathcal{O}$, $\mathcal{G}$, and $\mathcal{A}$ respectively, $\varepsilon(t)$ represents the pendulum oscillation angle with respect to the floater axis y_1 set in its center of mass (CoM), while the distance between the latter and the pendulum hinge has been defined d, and the length of the pendulum is l. With this configuration, the equation that regulates the pendulum motion is [1]:

$$\left(I_y+ml^2\right)\ddot{\varepsilon} - ml\cos(\delta+\varepsilon)\ddot{x} + ml\sin(\delta+\varepsilon)\ddot{z} + \left(I_y+ml^2-mdl\cos(\varepsilon)\right)\ddot{\delta} - mdl\sin(\varepsilon)\dot{\delta}^2 + mgl\sin(\delta+\varepsilon) + T_{ctrl} = 0, \tag{7}$$

where I_y and m are the inertia around the baricentric axis of the pendulum mass and the mass itself, while g is the gravity acceleration constant. The torque T_{ctrl} is the control torque applied on the pendulum oscillation axis. In this work, we supposed of working with an ideal PTO, able to directly exert the torque profile described by the control law that regulates T_{ctrl}. Under this ideal assumption, no losses that could affect the PeWEC productivity in the electrical conversion or given by the gearbox are considered. These, in a real PTO assumption will lead to further power losses (Sergiienko et al., 2022). Thus, the power absorbed by the PeWEC device is directly the mechanical one and it is given in its general formulation by:

$$P_{abs} = -T_{ctrl}\dot{\varepsilon}. \tag{8}$$

[1] From now on, the dependence on t is dropped when clear from the context.

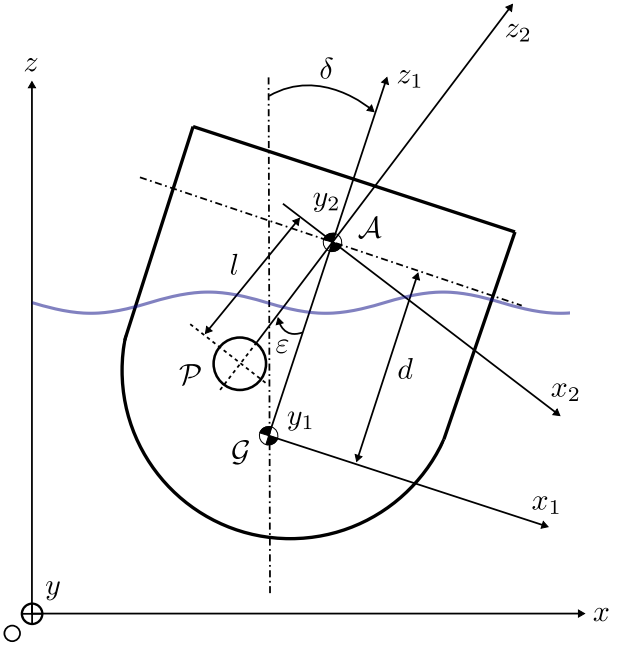

Figure 2: Scheme of PeWEC device.

It is worth noting that, in (8), being the T_{ctrl} acted at damping the pendulum motion, the power absorbed will have negative sign. The control torque T_{ctrl} is also related to the torque effectively generated by the PTO torque T_{PTO} by means of the gearbox ratio constant τ_{gear}:

$$T_{PTO} = \frac{T_{ctrl}}{\tau_{gear}}. \tag{9}$$

It is important to notice that, being the PTO a real generator, in the nonlinear case, it has been modelled with saturations on the maximum torque $T_{PTO,max}$ and on the maximum power $P_{PTO,max}$. Having described the pendulum dynamics, the pendulum forces F_{pend} acting on the hull can be defined as:

$$\begin{aligned}
F_{pend,x} &= -md\cos(\delta)\ddot{\delta} - ml\cos(\delta+\varepsilon)\left(\ddot{\delta}+\ddot{\varepsilon}\right) + md\sin(\delta)\dot{\delta}^2 - ml\sin(\delta+\varepsilon)\left(\dot{\delta}+\dot{\varepsilon}\right)^2 \\
F_{pend,z} &= +md\sin(\delta)\ddot{\delta} - ml\sin(\delta+\varepsilon)\left(\ddot{\delta}+\ddot{\varepsilon}\right) + md\cos(\delta)\dot{\delta}^2 - ml\cos(\delta+\varepsilon)\left(\dot{\delta}+\dot{\varepsilon}\right)^2 \\
F_{pend,\delta} &= T_{ctrl} + F_{pend,x}d\cos(\delta) - F_{pend,z}d\sin(\delta)
\end{aligned} \tag{10}$$

It is important to highlight that the whole model of the PeWEC device has been extensively validated in (Pozzi et al., 2018b) and (Pozzi et al., 2017). As it is possible to notice, the equations that regulates the PeWEC dynamics are characterized by several nonlinearities. This type of models are not suitable for control applications, being computationally expensive and time consuming. For this reason, a Jacobian linearized version is often adopted for control purposes. In the PeWEC case, the linearization assumes small oscillations around the pitch and the pendulum axis, i.e. $\delta \simeq 0$ and $\varepsilon \simeq 0$. With this type of assumptions, considering a state vector $X_{tot} = [x, z, \delta, \varepsilon]^T$ the system equations can be reduced in a matrix form to:

$$M_{tot}\ddot{X}_{tot} + B_{tot}\dot{X}_{tot} + K_{tot}X_{tot} + F_{r,tot}(\dot{X}_{tot}, \zeta_r) = F_{ext,tot}, \tag{11}$$

where the total inertia M_{tot}, the total damping B_{tot} and the total stiffness K_{tot} matrices are respectively:[2]

$$M_{tot} = \begin{bmatrix} M_{x,x} + A_{\infty_{x,x}} & 0 & A_{\infty_{x,\delta}} + m(d-l) & -ml \\ 0 & M_{z,z} + A_{\infty_{z,z}} & 0 & 0 \\ A_{\infty_{\delta,x}} + m(d-l) & 0 & M_{\delta,\delta} + A_{\infty_{\delta,\delta}} - 2mdl & I_y + ml^2 - mdl \\ -ml & 0 & I_y + ml^2 - mdl & I_y + ml^2 \end{bmatrix}, \tag{12}$$

$$B_{tot} = \begin{bmatrix} B_{v,lin_{x,x}} & 0 & 0 & 0 \\ 0 & 0 & 0 & 0 \\ 0 & 0 & B_{v,lin_{\delta,\delta}} & 0 \\ 0 & 0 & 0 & 0 \end{bmatrix}, \tag{13}$$

$$K_{tot} = \begin{bmatrix} 0 & 0 & 0 & 0 \\ 0 & K_{h_{z,z}} & 0 & 0 \\ 0 & 0 & K_{h_{\delta,\delta}} - mg(d-l) & mgl \\ 0 & 0 & mgl & mgl \end{bmatrix}, \tag{14}$$

where in (13) the terms $B_{v,lin_{x,x}}$ and $B_{v,lin_{\delta,\delta}}$ are viscous parameters obtained by the linearization of the nonlinear viscous terms. The force contributions $F_{r,tot}(\dot{X}_{tot}, \zeta_r)$ and $F_{ext,tot}$ are respectively:

$$F_{r,tot}(\dot{X}_{tot}, \zeta_r) = \begin{bmatrix} F_r \\ 0 \end{bmatrix}, \tag{15}$$

$$F_{ext,tot} = \begin{bmatrix} F_{wave} \\ -T_{ctrl} \end{bmatrix}. \tag{16}$$

As it is possible to notice from the previous equations, in the linearized version of the PeWEC model the mooring contribution is approximated for the sake of simplicity. We introduce this last linear version of the PeWEC model to present a model with lower accuracy with respect to the nonlinear one. This enable us to include the data coming from this computationally efficient model (in which the nonlinearities are approximated, and they are acting like an wrongly modelled behaviour of the real system, represented in our case study by the nonlinear model) as an incomplete and partially wrong knowledge of the system. The low-fidelity data are going to be produced offline and used by the strategy before starting the real learning process that is going to be performed online (and simulated on the nonlinear model in this work). It is also important to highlight that the linearized model is not used to perform power assessment. In fact, the nonlinear model is adopted to compute the real power in the control test. The only way in which the linearized model has been adopted is to produce approximated data used to speed up the convergence, by means of the multi-fidelity kriging approach able to deal with data with low fidelity (from the linearized model) and with higher fidelity (the real ones, represented in this case by the nonlinear simulations results) at the same time. The same approach could be adopted in a real world setting by substituting the previous 'wrong knowledge', played by the linear model, with data coming from models with higher fidelity, and next using experimental data coming from the real WEC as the source of highest fidelity data.

2.1. Case of study

We considered a PeWEC device with main characteristics defined in Tab. 1, coming from the previous works (Sirigu et al., 2020; Carapellese et al., 2021). This device has been designed to have a resonance frequency around 6 $[s]$, as it can be seen from the Response Amplitude Operator (RAO) in Fig. 3 allowing it to work effectively when placed in climates similar to the Mediterranean one. For this reason, we decided to simulate the effectiveness of the proposed control strategy adopting as site of deployment Alghero, in Sardinia, Italy. The data regarding the occurrences of the different sea-states have been taken from the data-set of RON (*Rete Ondametrica Nazionale*) on the *Linked ISPRA* website. A graphical representation of the percentage of occurrences in Alghero can be seen in Fig. 4. This percentage

[2]The notation $M_{i,j}$ is related to the M contribution of the j-th axis on the i-th one. The same is valid for A_∞ and K_h.

Table 1
Adopted PeWEC device: main characteristics.

Symbol	*Quantity*	*Value*
L_f	Floater Length	14.8 [m]
W_f	Floater Width	22.5 [m]
H_f	Floater Height	7.4 [m]
R_f	Floater Radius	7.4 [m]
D_f	Floater Draft	4.8 [m]
M_f	Floater Mass	1120000 [kg]
n_{pend}	Number of Pendulums	1
m	Pendulum Mass	71700 [kg]
l	Pendulum Length	2.4 [m]
d	Distance between Hinge and Hull CoM	2.5 [m]
I_y	Pendulum Inertia around y Axis	5100 [kgm^2]
$T_{PTO,max}$	PTO Maximum Torque	38 [kNm]
$P_{PTO,max}$	PTO Maximum Power	1000 [kW]
τ_{gear}	Gearbox Ratio	30

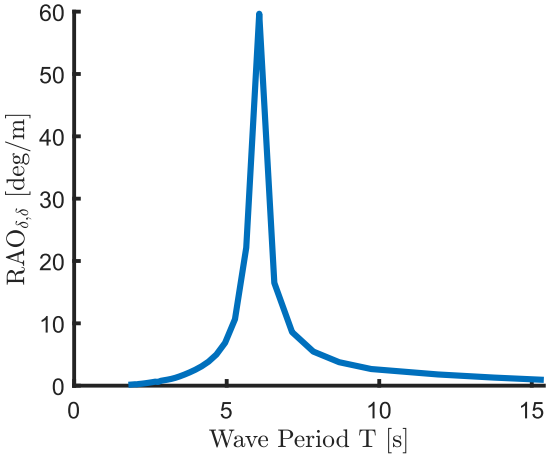

Figure 3: Response Amplitude Operator of pitch degree of freedom.

of occurrences corresponds to a probability distribution that was used to generate a month-long succession of sea states. Each sea state was assumed to last 30 minutes. This type of succession was then adopted to test the learning process that the proposed strategy is able to implement.

3. The Optimal Control Problem

In order to make PeWEC, and other WEC devices in general, feasible from an economic point of view, one of the fundamental problems to be solved is the development of a suitable control strategy (Ringwood, 2020). In fact, the control systems for WEC applications are responsible for the process of maximization of the absorbed energy, while also adapting to the different wave conditions that could occur in an environment like the sea or the ocean. A classical approach to do that in the unconstrained case is the so-called *impedance-matching* principle (Faedo et al., 2022). Moreover, a key factor for the reduction of the cost of energy is the minimization of human intervention for maintenance purposes, since WECs are usually placed offshore. For this reason, one of the aims of the suitable control strategy to be employed should be to avoid exceeding the structural limits imposed by the internal components of WECs. As it can be seen from the above objectives, the optimization process leading to the calculation of the optimal control

action is a constrained optimization process, commonly called WEC Optimal Control Problem (OCP) (Faedo et al., 2017). Models of the system are usually adopted to solve the OCP. By assuming that the adopted model is close to the real system behaviour and by means of model-based solutions, it is easier to compute directly the control force/torque to be employed. In wave energy field, different model-based optimal control strategies have been developed. Among them, the most popular are: model predictive control (MPC) (Li and Belmont, 2014; Hals, Falnes and Moan, 2011), moment-based control (Faedo et al., 2021b,a), spectral and pseudo-spectral methods (Garcia-Violini and Ringwood, 2021), and energy-maximizing linear time invariant controller (LiTe-Con)(Garcia-Violini et al., 2020; Carapellese et al., 2022). The control-oriented model adopted for in this type of optimization is a trade-off between the accuracy of system description, and the low complexity for optimality computation in real-time. As a result, the model adopted to describe the behaviour of the WECs to be controlled is characterized by a certain degree of inaccuracy and uncertainty (Ringwood et al., 2020). This type of problem can be solved by adopting a robust control approach (Garcia-Violini and Ringwood, 2021) or by pursuing a model-free strategy. In WEC control different model-free solution have been adopted, like extremum-seeking control (Parrinello et al., 2020; Garcia-Rosa et al., 2012; Moens de Hase et al., 2021), reinforcement learning (Anderlini et al., 2016, 2018, 2020; Zou et al., 2022), or neural-network control (Anderlini et al., 2017; Pasta et al., 2021a). It is worth noting that the work in Anderlini et al. (2020) offers a first example of using prior knowledge of a system model in a model-free control context. More in particular, the authors adopted a previously developed MPC based on a linear model of the system to accelerate the learning of a control based on reinforcement learning, avoiding also unpredictable WEC behaviour during the initial learning stage.

As stated before, the main objective of the control system in the WEC applications is the maximization of the energy extracted over a certain time interval $\mathcal{T} = [a, b] \subset \mathbb{R}^+$. Having defined the instantaneous absorbed power P_{abs} as in Eq. (8) in its general formulation, the control objective $\mathcal{J}$ may be formulated as:

$$\mathcal{J}\left(T_{ctrl}\right) = \frac{1}{L_{\mathcal{T}}} \int_{\mathcal{T}} T_{ctrl}(\tau)\, \dot{\epsilon}(\tau)\, d\tau, \tag{17}$$

where $L_{\mathcal{T}} = b - a$. The optimization process performed in the computation of the optimal control action is subject to the constraints that may be necessary to enforce on the device motion or on the control input, like the bound on the control action $T_{\mathrm{PTO},max}$ in the case of PeWEC. Hence, the optimal control action becomes the solution of the OCP:

$$T_{\mathrm{ctrl}}^{\mathrm{opt}} = \arg\max_{T_{\mathrm{ctrl}}} \left\{ \mathcal{J}\left(T_{\mathrm{PTO}}\right) \text{ s.t. : WEC dynamics, Motion and input constraints} \right\}. \tag{18}$$

The control strategy is responsible to solve such an optimization problem.

In the PeWEC application case, even if some initial attempts have been performed to move towards an optimization-based solution of the OCP (Pasta et al., 2021b), the current control strategy is the so-called *reactive control* (Maria-Arenas et al., 2019; Ringwood et al., 2014). The law adopted in this type of configuration is a feedback control law, in

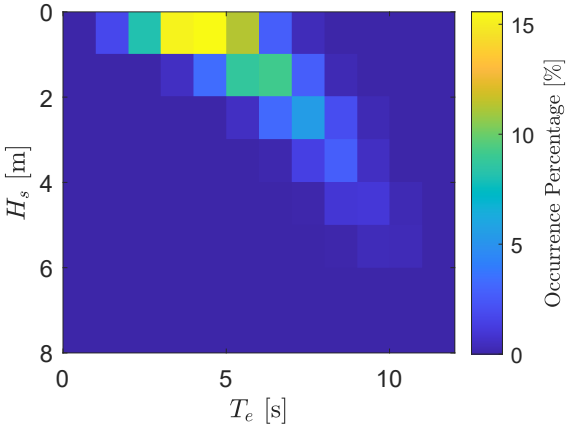

Figure 4: Occurrences scatter of the Alghero site (from RON data-set found on *Linked ISPRA* website).

which the control action is a linear combination of velocity and position on the conversion axis. In the PeWEC case this becomes:

$$T_{ctrl} = C\dot{\varepsilon} + K\varepsilon, \tag{19}$$

where the parameters C and K behave like a damping and stiffness contributions respectively. In real conditions, the constraints on the control action are not directly implemented with this type of simple control. For this reason, the torque T_{ctrl} is saturated when it exceeds the maximum allowed value. The optimal pair of parameters (C, K) is computed for each sea state by means of simulations that use the linear version of the PeWEC, checking a posteriori if the T_{PTO} exceeds the constraint, and discarding the control configurations that do not respect this bound. In particular, the chosen parameters for each sea-state are computed by means of a genetic algorithm aimed at maximizing the *Annual Energy Production* (AEP):

$$AEP = \frac{3600 \cdot 24 \cdot 365}{100} \sum_{w=1}^{N_w} Occ_{\%_w} P_{abs_w}(C_w, K_w), \tag{20}$$

where w is the index spanning the N_w sea-states with non-zero occurrence percentage $Occ_{\%_w}$, while $P_{abs_w}(C_w, K_w)$ is the average absorbed power in that wave condition when the control configuration (C_w, K_w) is applied. It is worth noting that also in the genetic optimization of the (C_w, K_w) parameters for each sea-state, the pair of damping and stiffness that lead to constraints violation are discarded. This optimization is based on the linear version of the PeWEC model to avoid overly long optimization times.

4. Optimization based on Gaussian process regression

Surrogate models are a popular solution to cope with optimization based on expensive computer simulations (Forrester and Keane, 2009; Jones, 2001). Their aim is to approximate a black-box function evaluated through deterministic or stochastic simulations, relying on a limited number of points and assuming some mild hypotheses on the analyzed phenomena. Among the widely used metamodeling (also known as surrogate model building) approaches we may mention *low-order polynomials* (Kleijnen, 2015), *Radial Basis Functions* (RBF) (Regis and Shoemaker, 2007), and *Gaussian Process Regression* (GPR), which may be considered as an extension of the *Kriging* approach, originally developed by Krige (1951) within the context of geostatistics applications. The application of GPR to a plethora of different scientific environments is continuously evolving and widening in scope (Kleijnen, 2009); indeed, GPR has also become a common tool in machine learning (Rasmussen and Williams, 2005). In this paper, we apply GPR metamodels to optimize the parameters of the control strategy of PeWEC.

Global optimization of black-box functions relies on metamodels (surrogate models) in different ways that differ with respect to both the specific kind of response surface adopted and the strategy to select search points in an effective way, to learn while keeping the computational effort to a reasonable level. A famous taxonomy of existing approaches was provided in Jones (2001); see also Forrester and Keane (2009) and Forrester et al. (2008) for a more recent and practical guide.

In order to outline our control approach, we first describe a simple GPR Bayesian approach, following the function-space oriented notation of Rasmussen and Williams (2005), in order to provide a glimpse of how the selected method accomplishes regression and prediction tasks.[3] Then we will present a generalization based on Multi-Fidelity (MF) data (also known as *co-kriging*), based on Forrester et al. (2007). This approach, referred to as MF-GPR, will be useful to exploit the simplified version of the system model when less common sea-states are encountered. Lastly, we will introduce the optimization framework, based on Forrester and Keane (2009) and Jones et al. (1998), that will be implemented with both GPR and MF-GPR metamodels.

4.1. Gaussian Process Regression

Let us consider a set of n joint observations

$$\mathcal{D} = \{(\mathbf{x}_i, y_i) : i = 1, \dots, n\}. \tag{21}$$

[3] Several different perspectives are possible to deal with GPR methodologies. This notation has been selected because the MATLAB implementation of GPR in the Statistics and Machine Learning Toolbox, which has been extensively used and adapted for the experiments of this project, follows this reference.

of the extracted power y_i for a set of control parameter settings $\mathbf{x}_i \in \mathbb{R}^d$. In our specific case study, $d = 2$ and each $\mathbf{x}_i$ denotes a pair of control parameters (C, K), for a proportional-derivative control. However, the idea is more general and the d parameters could be the coefficients of a functional to be optimized within a Model Predictive Control strategy. We aim to infer a (meta-)model $F(\mathbf{x})$, where we assume that the observed amounts of extracted power are random variables with a jointly Gaussian distribution. Formally, we assume that the nonlinear model of PeWEC will generate a sample of noisy responses, the extracted power, according to a data-generating process like

$$Y(\mathbf{x}) = F(\mathbf{x}) + \epsilon, \qquad \epsilon \sim \mathsf{N}(0, \lambda), \tag{22}$$

where $Y(\mathbf{x})$ is the random variable underlying the observations y_i, whereas $F(\mathbf{x})$ is a Gaussian process defined as

$$F(\mathbf{x}) \sim \mathsf{GP}(m(\mathbf{x}), k(\mathbf{x}, \mathbf{x}')), \tag{23}$$

which is completely characterized by the mean function

$$m(\mathbf{x}) = \mathbb{E}[F(\mathbf{x})], \tag{24}$$

and the covariance function

$$k(\mathbf{x}, \mathbf{x}') = \mathbb{E}[(F(\mathbf{x}) - m(\mathbf{x}))(F(\mathbf{x}') - m(\mathbf{x}'))]. \tag{25}$$

The essential idea behind Gaussian processes is that any sample of observations $\mathbf{x}_i$, $i = 1, \ldots, n$, has a joint normal distribution with expected values $m(\mathbf{x}_i)$ and a covariance matrix with entries $k(\mathbf{x}_i, \mathbf{x}_j)$, $i, j = 1, \ldots, n$. Specific assumptions on $m(\mathbf{x})$ lead to different flavors of kriging, i.e., *ordinary* or *universal* kriging. Ordinary kriging relies on a fixed (deterministic) mean function $m(\mathbf{x}) = \mu$, typically estimated through maximum likelihood, whereas in the universal version a regression model is built for the mean function. This distinction is well discussed in Kleijnen (2009) and Forrester and Keane (2009) from a viewpoint based on maximum likelihood estimation, and in Rasmussen and Williams (2005) from a Bayesian point of view. Given the lack of useful prior information, we will consider only the ordinary version. It is important to realize that the assumption of a constant mean is not a limitation, as predictions of a new value is actually dependent on the covariance function, which expresses the relationship between observations taken for similar values of $\mathbf{x}$.

The covariance function in classical kriging is

$$k(\mathbf{x}, \mathbf{x}') = \sigma^2 \exp\left(- \sum_{l=1}^{d} \frac{|x_l - x'_l|^{p_l}}{\theta_l} \right), \tag{26}$$

where each of the d components of $\mathbf{x}$ is associated with a scale parameter θ_l and an exponent p_l, whereas σ is related with the variance of the target variable. Such a large number of parameters makes the approach quite flexible, but calls for possibly difficult estimation procedures. Moreover, in engineering applications we may assume smoothness properties that are not guaranteed by every parameter setting. An alternative approach is common in kernel-based machine learning methods, and relies on kernel functions (Rasmussen and Williams, 2005; Stein, 1999).

In this paper, we experiment with the following three kernels:

1. The squared exponential kernel

$$k(\mathbf{x}, \mathbf{x}') = \sigma^2 \exp\left(-\frac{(\mathbf{x} - \mathbf{x}')^2}{2\theta} \right). \tag{27}$$

2. The Matérn52 kernel

$$k(\mathbf{x}, \mathbf{x}') = \sigma^2 \left(1 + \frac{\sqrt{5}r}{\theta} + \frac{5r^2}{3\theta^2} \right) \exp\left(-\frac{\sqrt{5}r}{\theta} \right), \qquad r = \|\mathbf{x} - \mathbf{x}'\|. \tag{28}$$

3. The ARD-Matérn52 kernel

$$k(\mathbf{x}, \mathbf{x}') = \sigma^2 \left(1 + \sqrt{5}r + \frac{5r^2}{3} \right) \exp\left(-\sqrt{5}r \right), \qquad r = \sqrt{\sum_{l=1}^{d} \frac{(x_l - x'_l)^2}{\theta_l}}, \tag{29}$$

where ARD stands for *Automatic Relevance Determination* and entails a separate length scale θ_l for each variable.

The first kernel consists of an infinitely differentiable radial basis function, and a very regular metamodel is obtained as a consequence. This kernel is the simplest version of the classical kriging, where the scale parameter θ is the same for each space direction and the exponent is fixed. A possible objection against such a simple kernel is that it implicitly assumes strong and possibly unrealistic hypotheses about the underlying physical phenomena. As an alternative, the use of of the Matérn family is proposed, e.g., in Stein (1999). We will compare the performance of the three alternatives in Section 5.

Given a structure for the covariance function, let us consider how the set of observations (21) can be used to predict performance. For a given kernel, we may consider the joint distribution of variables Y_p and Y_q, with covariance

$$\mathrm{cov}(Y_p, Y_q) = k(\mathbf{x}_p, \mathbf{x}_q) + \lambda^2 \delta_{pq}. \tag{30}$$

Here δ_{pq} is a Kronecker delta that takes into account a Gaussian noise, assumed independent identically distributed with a standard deviation λ, estimated by maximum likelihood and representative of the noise magnitude.

Let us collect the responses into the random vector $\mathbf{Y}$ ($\mathbf{y}$ when observed) and the control settings into matrix $\mathcal{X} = [\mathbf{x_1}, \dots, \mathbf{x_n}]$. Then we have

$$\mathrm{cov}(\mathbf{Y}) = \mathcal{K}(\mathcal{X}, \mathcal{X}) + \lambda \mathbf{I}_n, \tag{31}$$

where $\mathbf{I}_n$ is the $n \times n$ identity matrix and $\mathcal{K}$ is an operator associated with the selected Kernel function, such that $\mathcal{K} : \mathbb{R}^{d\times n} \times \mathbb{R}^{d\times n} \to \mathbb{S}^n_{++}$, where $\mathbb{S}^n_{++}$ denotes the space of the $n \times n$ symmetric positive definite matrices.[4] Practically speaking, this boils down to the covariance matrix itself.

Denoting by $f_i = f(\mathbf{x}_i)$ the observed values of the Gaussian process (differing from y because the noise is subtracted) and assuming $m(\mathbf{x}) = \mathbf{0}$ at this stage, when we have to predict a new value corresponding to a control setting $\mathbf{x}^*$, we arrive at the Gaussian process regression core

$$\begin{bmatrix} \mathbf{y} \\ F_* \end{bmatrix} \sim \mathcal{N}\left(\mathbf{0}, \begin{bmatrix} \mathcal{K}(\mathcal{X}, \mathcal{X}) + \lambda I_n & \mathcal{K}(\mathcal{X}, \mathbf{x}^*) \\ \mathcal{K}(\mathbf{x}^*, \mathcal{X}) & k(\mathbf{x}^*, \mathbf{x}^*) \end{bmatrix}\right). \tag{32}$$

Notice that $k(\mathbf{x}^*, \mathbf{x}^*)$ is a scalar value, whereas $\mathcal{K}(\mathbf{x}^*, \mathcal{X})$, with a slight abuse of notation, returns a vector in $\mathbb{R}^d$. Moreover, F_* is now a random variable associated with the value of interest f^*, i.e., the prediction corresponding to $\mathbf{x}^*$.

The multivariate Gaussian random variable has a well-known analytical formula for the distribution of a subset of variables, conditional on the realization of the remaining ones [a clear explanation is reported in (Rasmussen and Williams, 2005, Appendix A.2)]. By applying this formula, it is possible to retrieve the prediction of the model as

$$\begin{aligned} F_* | \mathbf{x}^*, \mathcal{X}, \mathbf{y} \sim \mathcal{N}(&\mathcal{K}(\mathbf{x}^*, \mathcal{X})[\mathcal{K}(\mathcal{X}, \mathcal{X}) + \lambda I_n]^{-1}\mathbf{y}, \\ &k(\mathbf{x}^*, \mathbf{x}^*) - \mathcal{K}(\mathbf{x}^*, \mathcal{X})[\mathcal{K}(\mathcal{X}, \mathcal{X}) + \lambda I_n]^{-1}\mathcal{K}(\mathcal{X}, \mathbf{x}^*). \end{aligned} \tag{33}$$

Hence, the required prediction is obtained as the mean value of F_*:

$$\bar{f}^* = \mathcal{K}(\mathbf{x}^*, \mathcal{X})[\mathcal{K}(\mathcal{X}, \mathcal{X}) + \lambda I_n]^{-1}\mathbf{y}. \tag{34}$$

Incorporating a fixed mean function $m(\mathbf{x}) = \mu$, estimated by maximizing the log-likelihood function, the predictive mean becomes

$$\bar{f}^* = \mu + \mathcal{K}(\mathbf{x}^*, \mathcal{X})[\mathcal{K}(\mathcal{X}, \mathcal{X}) + \lambda I_n]^{-1}(\mathbf{y} - \mathbb{1}\mu), \tag{35}$$

where $\mathbb{1} = [1, \dots, 1]^\mathsf{T} \in \mathbb{R}^n$. Besides the mean, the prediction of the model in (33) provides the covariance of f^*. This further value is related to one of the key advantages of the GPR, namely an analytical estimation of the errors associated with the Gaussian hypothesis.

[4] The positive definiteness and the symmetry of this matrix depends on the kernel function. If the latter is radial and strictly positive definite, these two properties, required for a covariance matrix, are fulfilled. The Bochner's theorem and the Schoenberg's one ensure this conditions for our selected kernels. For further details we refer to Fasshauer (2007).

4.2. Multi-Fidelity GPR

In our case study, we have two different levels of accuracy of the data, namely a linear and a nonlinear one. Let us consider two families of n_{l} and n_{nl} observations $\mathcal{X}_{\mathsf{l}}$ and $\mathcal{X}_{\mathsf{nl}}$, linear and nonlinear respectively, and let us rename the observation matrix, collecting control settings, and the corresponding responses as

$$\mathcal{X} = (\mathcal{X}_{\mathsf{l}}, \mathcal{X}_{\mathsf{nl}}), \qquad \mathbf{y} = (\mathbf{y}_{\mathsf{l}}, \mathbf{y}_{\mathsf{nl}}). \tag{36}$$

The typical assumption on multi-fidelity model can be traced back to Kennedy and O'Hagan (1998), who consider an auto-regressive model driven by a scaling factor ρ estimated by maximizing the log-likelihood.

If we denote by F_{l} and F_{nl} the Gaussian processes that represent the local features of the linear and nonlinear models, respectively, according to (23), we may combine the models by using the autoregressive-like process

$$F_{\mathsf{nl}}(\mathbf{x}) = \rho F_l(\mathbf{x}) + F_\Delta(\mathbf{x}), \tag{37}$$

where $F_\Delta(\mathbf{x})$ represents the process of the differences between ρF_{l} and F_{nl}. This model assumes that:

- The control designs evaluated by the nonlinear model are a subset of those evaluated by the linear model[5], i.e., $\mathcal{X}_{\mathsf{nl}} \subseteq \mathcal{X}_l$.
- If we have the nonlinear observations for a given configuration, no more information can be extracted about them from the corresponding linear. Thus,

$$\mathrm{cov}(Y_{\mathsf{l}}(\mathbf{x}), Y_{\mathsf{nl}}(\mathbf{x}) | Y_{\mathsf{nl}}(\mathbf{x})) = 0. \tag{38}$$

Let us adopt a different kernel for each fidelity $\mathcal{K}_{\mathsf{l}}$ and $\mathcal{K}_{\mathsf{nl}}$ and also different noise terms λ_{l}, λ_{nl} respectively. We will now have a new covariance matrix $C \in \mathbb{S}_{++}^{(n_{\mathsf{l}}+n_{\mathsf{nl}})}$, similar to $\mathcal{K}$ when we deal with a single model, that we can introduce by its blocks:

$$\mathrm{cov}(\mathbf{Y}_{\mathsf{l}}(\mathcal{X}_{\mathsf{l}}), \mathbf{Y}_{\mathsf{l}}(\mathcal{X}_{\mathsf{l}})) = \mathcal{K}_{\mathsf{l}}(\mathcal{X}_{\mathsf{l}}, \mathcal{X}_{\mathsf{l}}) \tag{39}$$

$$\mathrm{cov}(\mathbf{Y}_{\mathsf{nl}}(\mathcal{X}_{\mathsf{nl}}), \mathbf{Y}_{\mathsf{l}}(\mathcal{X}_{\mathsf{l}})) = \rho\mathcal{K}_{\mathsf{l}}(\mathcal{X}_{\mathsf{nl}}, \mathcal{X}_{\mathsf{l}}) \tag{40}$$

$$\mathrm{cov}(\mathbf{Y}_{\mathsf{nl}}(\mathcal{X}_{\mathsf{nl}}), \mathbf{Y}_{\mathsf{nl}}(\mathcal{X}_{\mathsf{nl}})) = \rho^2\mathcal{K}_{\mathsf{l}}(\mathcal{X}_{\mathsf{nl}}, \mathcal{X}_{\mathsf{nl}}) + \mathcal{K}_{\mathsf{nl}}(\mathcal{X}_{\mathsf{nl}}, \mathcal{X}_{\mathsf{nl}}) \tag{41}$$

from which we obtain

$$C(\mathcal{X}, \mathcal{X}) + \lambda = \begin{bmatrix} \mathcal{K}_{\mathsf{l}}(\mathcal{X}_{\mathsf{l}}, \mathcal{X}_{\mathsf{l}}) + \lambda_{\mathsf{l}} I_{n_{\mathsf{l}}} & \rho\mathcal{K}_{\mathsf{l}}(\mathcal{X}_l, \mathcal{X}_{\mathsf{nl}}) + \lambda_{\mathsf{l}} \begin{pmatrix} \mathbf{0}_{n_{\mathsf{l}}-n_{\mathsf{nl}} \times n_{\mathsf{nl}}} \\ I_{n_{\mathsf{nl}}} \end{pmatrix} \\ \rho\mathcal{K}_{\mathsf{l}}(\mathcal{X}_{\mathsf{nl}}, \mathcal{X}_{\mathsf{l}}) + \lambda_{\mathsf{l}} \begin{pmatrix} \mathbf{0}_{n_{\mathsf{nl}} \times n_{\mathsf{l}}-n_{\mathsf{nl}}} & I_{n_{\mathsf{nl}}} \end{pmatrix} & \begin{bmatrix} \rho^2(\mathcal{K}_{\mathsf{l}}(\mathcal{X}_{\mathsf{nl}}, \mathcal{X}_{\mathsf{nl}}) + \lambda_{\mathsf{l}} I_{n_{\mathsf{l}}}) \\ + (\mathcal{K}_{\mathsf{nl}}(\mathcal{X}_{\mathsf{nl}}, \mathcal{X}_{\mathsf{nl}}) + \lambda_{\mathsf{nl}} I_{n_{\mathsf{nl}}}) \end{bmatrix} \end{bmatrix}. \tag{42}$$

Following the same structure of the single-fidelity case, the predictor will now be

$$\bar{f}^* = \mu + C(\mathbf{x}^*, \mathcal{X})[C(\mathcal{X}, \mathcal{X}) + \lambda]^{-1}(\mathbf{y} - \mathbb{1}\mu). \tag{43}$$

A deeper explanation of the analytical steps and the properties of the kernel matrix C is not presented here for the sake of brevity, and the interested readers are referred to Forrester et al. (2007).

4.3. The optimization framework

The general framework that is typically adopted for the surrogate optimization can be divided in the following steps:

Step 1. Some initial points on the control space are selected to provide an explorative view. This step is based on a *initial sampling* strategy where the only available information is the problem domain.

Step 2. The initial surrogate model is built by using the initial points and the selected metamodel features.

[5] If the data do not satisfy this condition, it can be tackled by using kriging estimates to complete the structure.

Step 3. One or more new points are selected according to an *acquisition strategy* that exploits all the points of the surrogate model involved so far and the current model features.

Step 4. The simulation is run on the selected points, obtaining new observations that are used to update the surrogate model. The new surrogate model is estimated on the basis of all of the previous observations and the new one/ones.

Step 5. The procedure is iterated from Step 3. until an exit criterion (typically a time constraint) is reached.

The first matter that must be clarified concerns the *acquisition strategy*. As previously mentioned, we will follow Jones et al. (1998), whose *Efficient Global Optimization* (EGO) algorithm exploits Gaussian Process Regression, providing an automated balancing of exploration and exploitation in the search of the new point to be evaluated, avoiding the local minima that may be generated by a pure exploration strategy. The idea relies on selecting the point with the highest expected improvement with respect to the available information about the Gaussian Process. More specifically, assuming a standard minimization problem,[6] we can predict the response for a point $\mathbf{x}^*$ in our metamodel by $\bar{f}^*$ and our setting will also provide an associated standard deviation s^* of the predictor based on the Gaussian assumptions. If we introduce a new random variable

$$I(\mathbf{x}) = y_{\min} - Y(\mathbf{x}) \tag{44}$$

that models the improvement with regards to our actual observed minimum $y_{\min}$, by exploiting the Gaussian assumption, the expected improvement of a selected $\mathbf{x}^*$ will be

$$\mathbf{E}[I(\mathbf{x}^*)] = \begin{cases} (y_{\min} - \bar{f}^*)\,\Phi\left(\frac{y_{\min}-\bar{f}^*}{s^*}\right) + s\,\phi\left(\frac{y_{\min}-\bar{f}^*}{s^*}\right) & s^* > 0 \\ 0 & s^* = 0 \end{cases}, \tag{45}$$

where Φ and ϕ are the cumulative and probability density functions of the Gaussian distribution, respectively.

Regarding the *initial sampling*, we have adopted *Latin Hypercube Sampling* (LHS) in two flavors. When we consider a single fidelity environment, LHS is used in their common form, but, when two fidelities are available, the sampled points of the nonlinear fidelity model will be a subset of the linear one and they will be selected according to the Morris and Mitchell criterion. A deep explanation of these methods is available in Forrester et al. (2008).

The exit criterion, when we compute expensive simulations or real data, is typically forced by the time or the availability. Although it is possible to set a tolerance after which the improvement is small enough and meets a satisfaction criterion, we will perform as many iterations as we can within a reasonable computational budget.

5. Kernel selection

As we have already mentioned, kernels will be the main players in the regression approach, as they incorporate our prior assumptions on the smoothness of the metamodel that describes the PeWEC power extraction with respect to different control designs. There is a huge number of possible kernels and it is also possible to generate more kernels from existing ones by some specific operations that maintain their required characteristics (Rasmussen and Williams, 2005). We compare here the three alternatives described in Sect. 4.1. It is possible to test other kernels with the same methodology and framework, and it is important to test their sensibility with respect to the properties of the PeWEC device and to understand the effect of the alternative choices. The single or multiple dimensions scale parameters are estimated by maximizing the log-likelihood; thus, the potential advantages of a larger number of degrees of freedom is compensated by increasing optimization difficulties.

5.1. Single sea state example

In order to get a grasp of the effects of kernel selection, let us consider a single sea state w characterized by the following parameters: $H_s = 1.5$, $T_e = 3.5$, 30 minutes of power evaluation time. The number of points needed to find a reasonable surface are a subject of discussion. We refer to Loeppky, Sacks and Welch (2009) for different experiments on simple kriging, where $n = 20$ is suggested as suitable choice. Our kernels are different from the original methodology, but this number is also bounded by the time needed to carry out the system simulations and it turns to be a sensible one in our setup too.

[6] In our problem we seek to extract as much power as possible, thus we minimize the negative value of the extracted power.

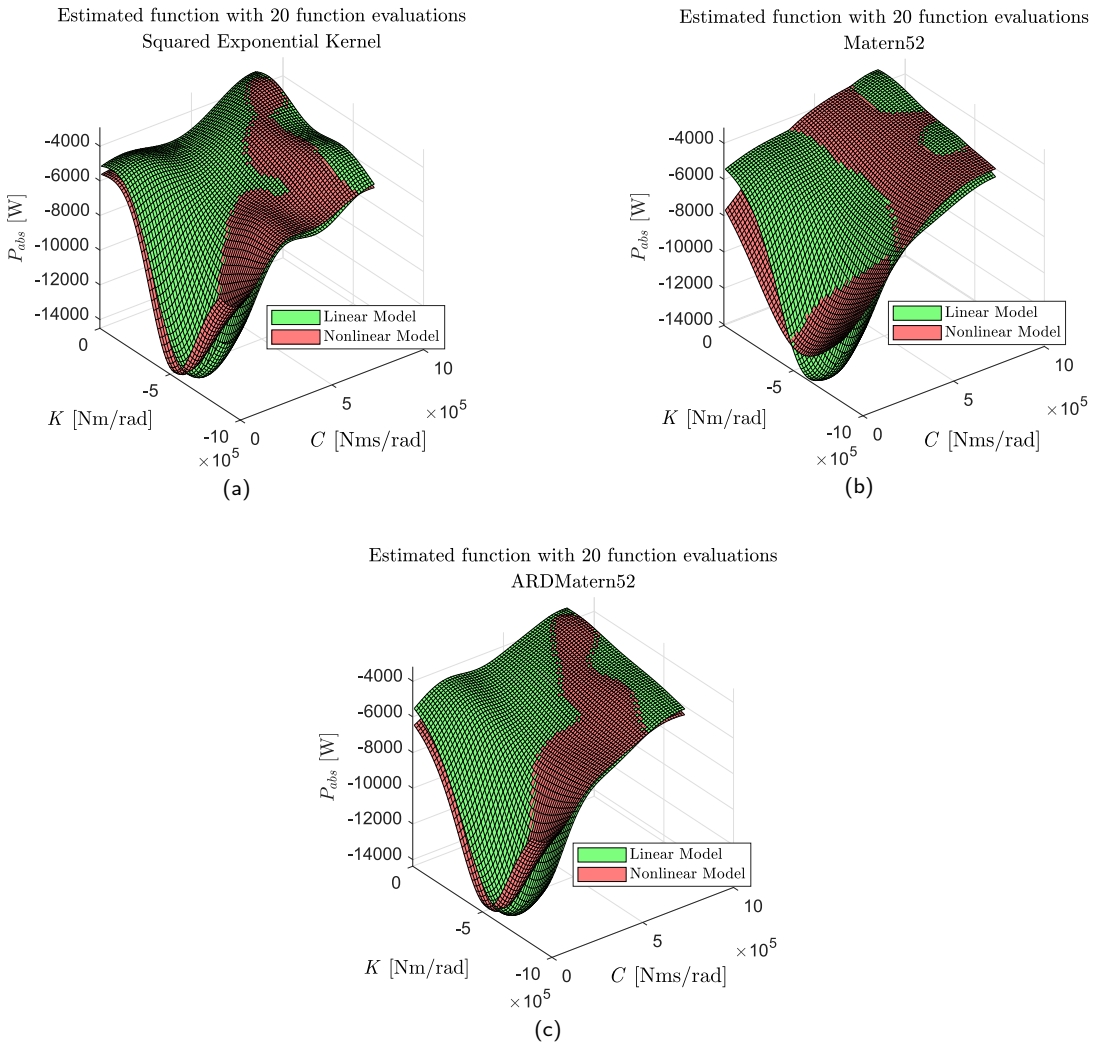

Figure 5: Gaussian Process Regression of Linear and Non Linear metamodel with different Kernels ($H_s = 1.5$ [m],$T_e = 3.5$ [s]).

Our problem involves noisy surfaces for the nonlinear model, whereas the linear one is assumed to be noise-free. This assumption identifies the two kernel settings for the linear and nonlinear model respectively. They will be practically the same, except that no noise is modelled for the linear one, thus we force $\lambda \simeq 0$ in (32).[7] The tuning of these kind of hyperparameters is a recurring question in machine learning applications and a deeper discussion on this aspect for PeWEC will be presented in the Sect. 6.

For both the linear and the nonlinear models, we fit their associated metamodel with the same set of 20 simulated points for all of the kernels. The algorithm will be the GPR, whereas the MF-GPR will become a main player in Sect. 6. The regressions have been performed in MATLAB with the Statistics and Machine Learning Toolbox, where the previously presented formulation is implemented.[8] In Fig.7, the plot of the different kernel results are shown and we notice several clear differences between the metamodels. More specifically, a higher dissimilarity is visible among regressions with the nonlinear simulation model, displayed in red, as is expected because of the noise. On the other hand, the predictions for the linear simulation model, displayed in green, tend to maintain their shape throughout the

[7] When no noise is modelled, this value is set to a small positive number to avoid heavily ill-conditioned covariance matrices by a regularization effect.

[8] Different implementations of the Gaussian Process Regression algorithm can generate different results (Erickson, Ankenman and Sanchez, 2018). In the description of the methods, we have described a specific algorithm that fits the software implementation.

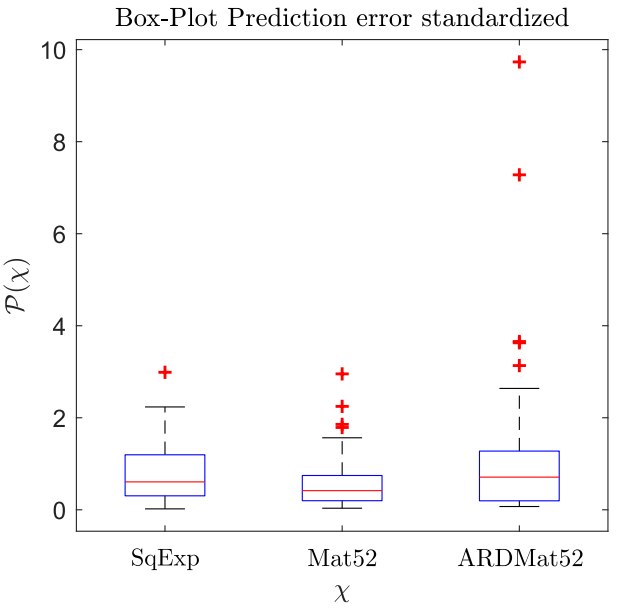

Figure 6: Box-Plot of the maximum of the Prediction Error Standardized for each kernel

experiments.

5.2. Kernel selection

Armed with an intuitive and graphical feeling for the impact of kernel choice on modeling in a single sea state, the next question is how to select the right one. In order to evaluate the fitting properties of regression models, one of the widely adopted strategies in machine learning is cross-validation, possibly the *Leave One Out Cross Validation* (LOO-CV) version. Specifically for GPR models, we can adopt a particular form that takes into account the analytical estimation of the prediction of the variance (Kleijnen and Beers, 2019).

Let us define the *Prediction Error Standardized* (PES)

$$\mathrm{PES}_i = \frac{y_i - \bar{f}^{-i}}{s^{-i}}, \qquad i = \{1, \dots, n\}, \tag{46}$$

where y_i is the actual extracted power when applying the control setting $\mathbf{x}_i$, $\bar{f}^{-i}$ is the prediction of $\mathbf{x}_i$ by the metamodel built with $n-1$ observations, leaving out of the sample the i-th observation, with associated estimated standard deviation of s^{-i} based on the Gaussian assumptions.

The reader should not be tempted to use these raw values as performance indicators, since they are statistically dependent, because they use common data. A ready-to-use solution relies their distribution of maximum. For each sea state w and for each Kernel χ we consider

$$p(w, \chi) = \max_{i=1,\dots n} |\mathrm{PES}_i^{\chi}|, \tag{47}$$

where the set of indices $i = 1, \dots, n$ depends on sea state w and identifies the set of observations for that specific sea state.

In Fig.6, we show some descriptive statistics based on box-plots of $\mathcal{P}(\chi) = \left\{ p(w, \chi), \forall w \text{ s.t. } Occ_{\%_w} \neq 0 \right\}$, that represent the set of the maximum values for each kernel, for all of the available sea states. We may observe that the best kernel, among the three we consider, is *Matérn52*, since its empirical distribution of the maximum errors has lower statistics on the sea states. It must be also remarked that its ARD version, even though more flexible, provides really high maximum LOO-CV errors. This could be due to issues in the estimation of the parameters $\theta_j, j \in 1, \dots, d$. For the rest of this work we will use only the best kernel according these performance measures. Needless to say, there is room for further and deeper research on alternative kernels, but our aim is just to assess the value of the overall methodology.

6. Design of the learning experiment

After the specification of the GPR surrogate modeling appproach, we can introduce our control data-driven optimization for PeWEC. In Sect. 6.1 we test the convergence properties of the proposed strategy to the analytical optimal parameters, testing the strategy under regular wave and linear model conditions. In Sect. 6.2 we will study the performance of the optimization itself by assuming a mild limitation on the number of observations per sea state. In Sect. 6.3, on the contrary, we will discuss a more realistic experiment and the suggested methodology, when the observed sea states are determined by their occurrence distribution, with no ad hoc selection aimed to explore all the sea state space uniformly, starting with very little information and exploiting the MF-GPR approach.

6.1. Preliminary convergence analysis of a linear model under regular wave conditions

The first experiment that we perform aims at demonstrating the ability of the proposed strategy at converging to the optimal parameters in a simpler example, maximizing the extracted power. Here we test the control of a linear model of the system when excited by regular waves. Under these assumptions, the optimal control parameters are those able to ensure the impedance-matching conditions, that, for multi-DoF WEC devices like PeWEC, can be analitically computed as shown by the authors in (Faedo et al., 2022). Fixing the same sea-state condition employed in Sect. 5.1 (*e.g.* H_s=1.5[m], T_e=3.5[s]), we perform 20 initial explorative actions selected according to LHS. On the basis of the information thus obtained, adopting the strategy described in Sect. 4 and selecting the *Matérn52* kernel, 40 new control actions are chosen in the same sea-state conditions. The average power is evaluated every 30 minutes.

The results of the experiment are illustrated in Fig. 7a, 7b, and 7c, where the strategy is able to suitably converge to the optimal parameters after 10-15 new evaluations. Moreover, as shown in Fig. 7c, around the 7-th evaluation the expected power by the meta-model and the simulated one converge. Specifically, since the expected power is what the surrogate model of the power forecasts, the convergence effect entails the goodness of the model itself.

6.2. Optimization results

Let us now consider a GPR metamodel for each individual sea state, based on 20 points sampled according to LHS and simulated with the nonlinear model. This initial set of observations comprises an explorative view of the PeWEC behaviour with different control settingss. The idea is to perform the EGO optimization discussed in Sect. 4.3 with a fixed number of iteration per sea state. This experiment aims to point out some peculiar characteristics of this kind of optimization and to prove that improvement in the extracted power is provided.

For each optimization iteration, we compute the performance through the Annual Energy Production (AEP), assuming the optimization was stopped and the PeWEC system was launched with the sea states coherent with the presented distribution (Fig.4), operating according to the control strategy determined so far. In each loop, we add exactly one point for each sea state according to the EGO strategy.

To better clarify this approach, which is similar to what we use later, in Fig.8 we provide a graphical scheme of the overall framework. In the right portion of the scheme, the base framework reflects the algorithm of Sect. 4.3, including a new point for each sea state observation, whereas, in the left portion, we select the *here-and-now* optimized control according to our current metamodel, and then we simulate the AEP. Strictly speaking, the nonlinear model will be noisy, hence we re-assess the AEP three times for each evaluation.[9]

Another quantity of interest is the *expected AEP* (e-AEP). In fact, we compute the AEP with the deterministic minimum of the regressed surfaces that will differ from the noisy nonlinear simulation. This index represents the annual productivity that would be observed if for each sea state characterizing the site in which the PeWEC device is deployed, the control chosen by the optimization strategy is fixed and adopted for an entire year. It supplies fundamental information on the discrepancy between what can be extracted according to the metamodel and the actual performance. In Fig.9 we use the following representation:

- The black stars are the three simulated AEP for each optimization iteration.
- The blue points are the e-AEP of the metamodel.
- The grey lines are the AEP of a the reactive control optimized by a genetic algorithm using the **linear** model and

[9]This approach will not be possible anymore when the simulations are not managed by us at will, but are driven by the distribution of sea state occurrences.

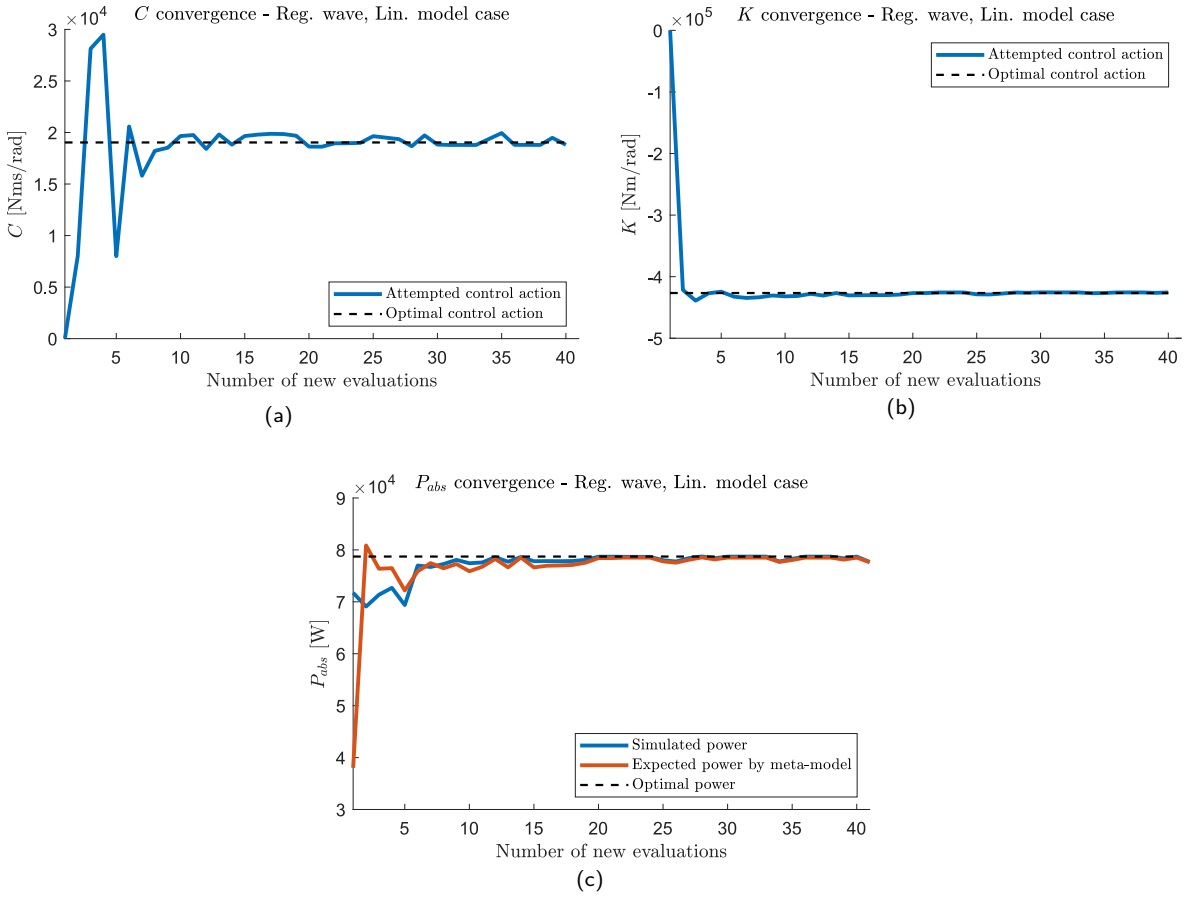

Figure 7: Convergence of the proposed strategy to the optimal parameters under regular wave conditions ($H_s = 1.5$ [m],$T_e = 3.5$ [s]).

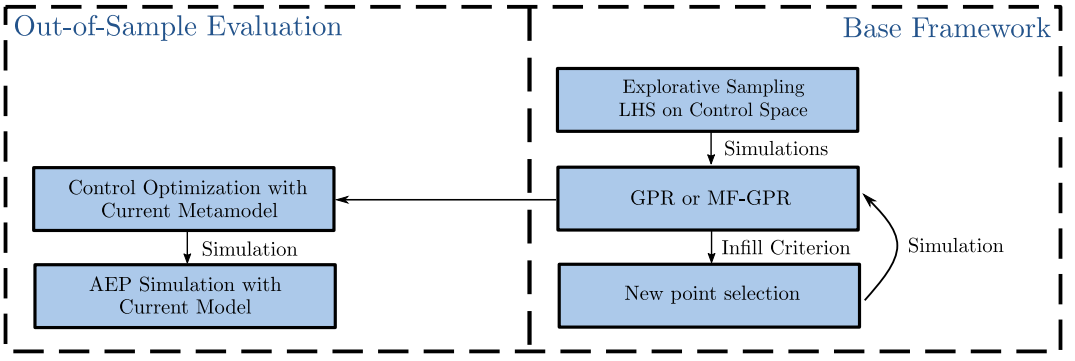

Figure 8: Experiment framework. In the right side the basic Gaussian process idea is outlined. On the other hand, an optimized simulation is step-wise provided to catch the performance improvements.

evaluated according to the **nonlinear** simulation model.[10]. These lines are three different AEP computations and the red one is their mean.

- The magenta line is the linear spline interpolation of the means of the simulated AEP.

[10]We recall that, due to the model complexity and to the time required for each simulation, the genetic algorithm is not applicable to the nonlinear model.

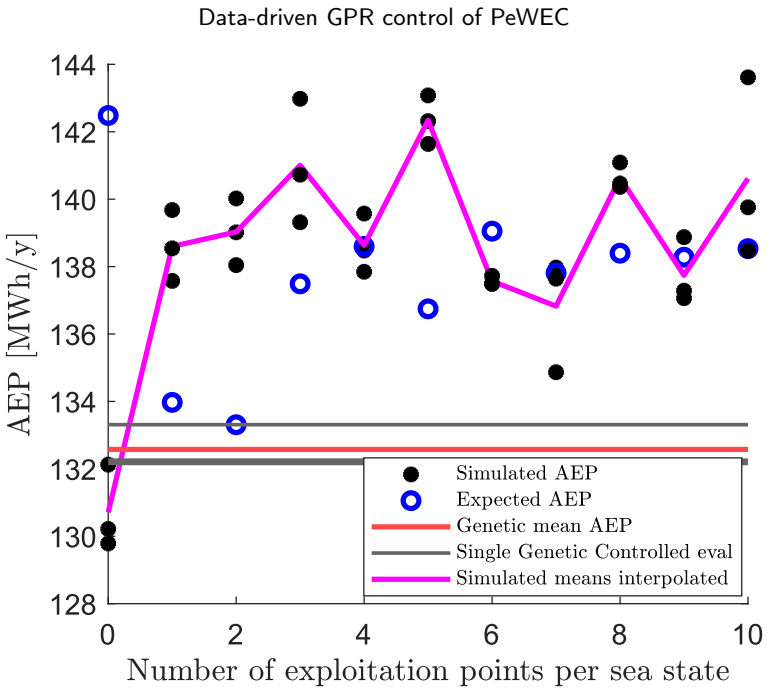

Figure 9: Optimization effect analysis on the simulated AEP and the expected AEP with a genetic control benchmark.

It is easy to note that the very first optimization loop is sufficient to outperform the Genetic benchmark, but the reader might wonder why the optimization behaviour is not constantly increasing. Two possible answers involve:

- The discrepancy between the AEP and the e-AEP.
- The noise of the nonlinear model.

Concerning the latter observation, the number of simulations per loop could be increased, but this is beyond of the scope of the present analysis. The main matter that we want to discuss is the continuous shrinking of the difference between AEP and e-AEP, showing that the optimization is somehow still learning and improving the metamodel. This phenomenon is indeed a fundamental feature of this approach, showing how the optimization approach takes into account its knowledge of the real phenomena and adapts itself progressively. This peculiarity of the GPR serves well the need for adjustments in the learning process for plants that are supposed to work for a long period of time, as we further illustrate in the next section.

For the sake of completeness, we show the optimization effect on the single sea state analyzed in Fig.5b, where the kernels were discussed. In Fig.10 the updated version of the metamodel is given. The old nonlinear surface is depicted in red, together with the LHS points, the updated nonlinear metamodel is depicted in green, and the points selected by the EGO strategy are depicted in blue. Although some points are near the presumed optimal control, some of them are placed quite far away, near the boundaries, with the aim of improving the regression. This result is an evidence of the exploration–exploitation trade-off implicit in the method.

A further comment concerns the initial number of explorative points. Even if the updated overall function shape features visible variations, the optimal region was correctly identified on the basis of the 20 initial points.

6.3. MF-GPR control at work

In real applications, it is not possible to simulate the sea states according to the learning necessity, but we are forced to follow the sea behaviour. Even the prior information of 20 initial nonlinear points could be excessively restrictive. In the simulation presented here, each control action is evaluated in terms of average power absorption every 30 minutes. These observations are very prominent when the role of the nonlinear (expensive) simulation model is played by real data, so that higher computational power is of no use and we need a methodology that makes the most of the available data. A low-fidelity model, such as the linear simulation model in our setting, could help avoiding to

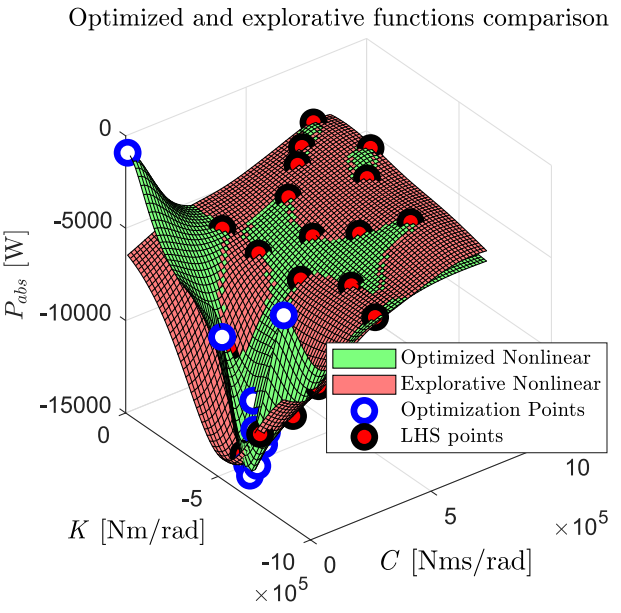

Figure 10: Single sea state optimization effect on the metamodel shape and on the new point selection (H_s = 1.5 [m],T_e = 3.5 [s]).

start from nowhere. As an example, in the case of a single sea state with low occurrences (T_e=9.5 [s],H_s=3.5 [m]), we show in Fig.11 the resulting metamodel by MF-GPR with 20 linear points and only 6 nonlinear ones.

More specifically, we plot the surface obtained by 20 points resulting from simulations of the linear model, the surface obtained by 20 simulations of the nonlinear model, and the multi-fidelity (CoKriging) with the 20 linear evaluations and a subset of 6 points also evaluated by the nonlinear model. What we notice is that the new metamodel is lifted with respect to the linear regression and lies between the two.

This example considers 6 nonlinear points as the minimum achievable prior explorative information, but this value, especially in the real applications, is led by the data and not by a fitting strategy. Moreover, the sea states have deep differences in their probabilities and sometimes a multi-fidelity approach is even redundant. This strategy is not meant to deal with an equal number of linear and nonlinear simulation and, when this happens, the linear model acts as additional noise on the regression.

The above-mentioned problem could be solved by an adaptive number of low-fidelity evaluation with respect the expected high-fidelity sea state control data, but this would lead to a big number of points for really common states and to further issues with the computational cost of large scale optimization. This matter is beyond the scope of this work and we rather prefer to bridge the initial knowledge of the Gaussian Process Regression control in the very initial phase of a possible real application, starting from uniform initial conditions for the sea states and dynamically adjusting the strategy taking data availability into account.

Let us suppose an initial condition of a set of MF-GPR for each sea state made by 20 low-fidelity simulations and only 6[11] high-fidelity control responses chosen according to the sampling methodology explained in Sect. 4.3. We now simulate a time period of one month, sampling sea states from the distribution presented in Sect. 2. Each high-fidelity extracted value will be also simulated in the low-fidelity model to fulfill the subset assumption of the auto-regressive model. When the number of high-fidelity observations is close to the low-fidelity ones, we dynamically switch the MF-GPR to a GPR with only the high-fidelity points. In particular, the Regression block of Fig.8 will contain the following sub-steps:

Step 1. If the the number of high-fidelity points is above a threshold, the GPR is performed.

Step 2. If the the number of high-fidelity points is below the threshold, the new high-fidelity control is simulated also in the low-fidelity model to maintain the auto-regressive subset hypothesis. Then a MF-GPR is performed.

[11] These assumption can be managed in respect of the data availability.

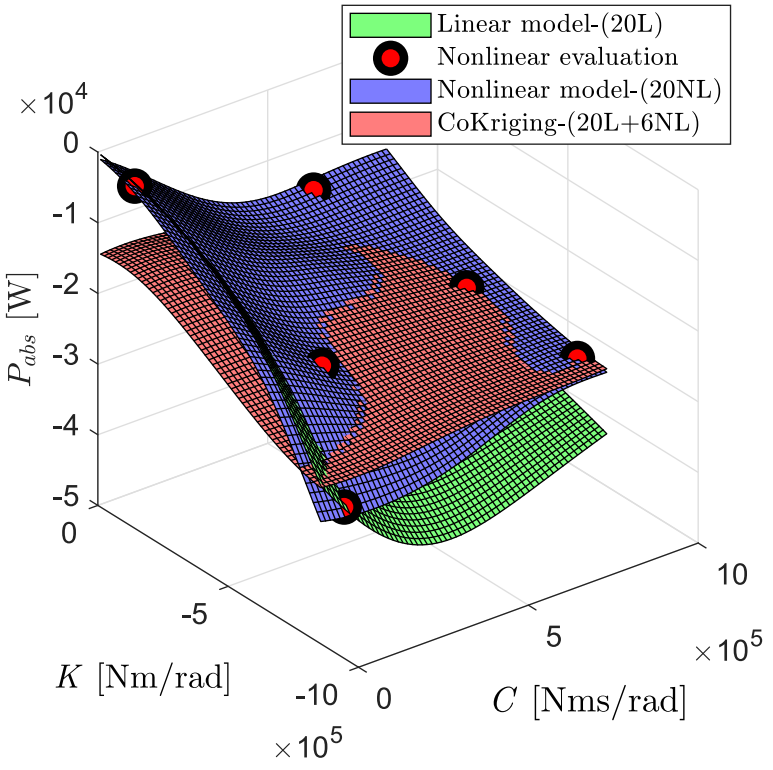

Figure 11: Single sea state MF-GPR ($H_s = 1.5$ [m],$T_e = 3.5$ [s]). In green the linear metamodel with 20 points, in blue the nonlinear one with the same controls and in red a Co-Kriging model with only 6 nonlinear evaluation added to 20 linear ones, represented as red bubbles.

In this specific example, we still rely on 20 high-fidelity points as a sufficient starting point for the GPR, but we remark that now these points are not all selected according to LHS, but only 6 of them are full explorative. The metamodel strategy will adjust itself automatically according to the exploration–exploitation trade-off. With this hypothesis, when the MF-GPR will be substituted by the full GPR, we have:

- 20+14 = 34 low-fidelity points
- 20 high-fidelity points ∼ 60% w.r.t. low ones

A summary of the simulation result is given in Fig.12, where the blue line is the AEP, the orange one the e-AEP, and the grey one is the Genetic benchmark previously considered in Sect. 6.2. The AEP quantities are computed by an average over a sliding window of length 43 across neighboring elements.[12] This representation has been chosen to deal with noise, since now we assume that the role of the nonlinear simulation model could be replaced by data, where controlled re-simulation is impossible. Since each evaluation corresponds to 30 minutes, the overall experiments will consider 1344 simulations.

From the starting point to around the 400-th evaluation, we observe the AEP/e-AEP discrepancy shrinking effect already seen in Fig. 9; after that, the optimization effect becomes clearly visible also in term of improvement in extracted power. At the end of simulated month, the expected improvement is around 12%, even if some sea conditions have been observed a couple of times, due to their low occurrence probability. This consideration is observable also in Fig. 13. There, we plot the set of regression for the discretized sea states (Fig.4), and the states with a relatively high number of high-fidelity observations coincides with the occurrence distribution, but the MF-GPR controls are good enough to provide good results by the AEP. However, in the lowest occurrence wave conditions, the amount of real experience is

[12] This number is the number of non zero sea states of the distribution matrix and it is not particularly meaningful. Similar plots are possible with different windows.

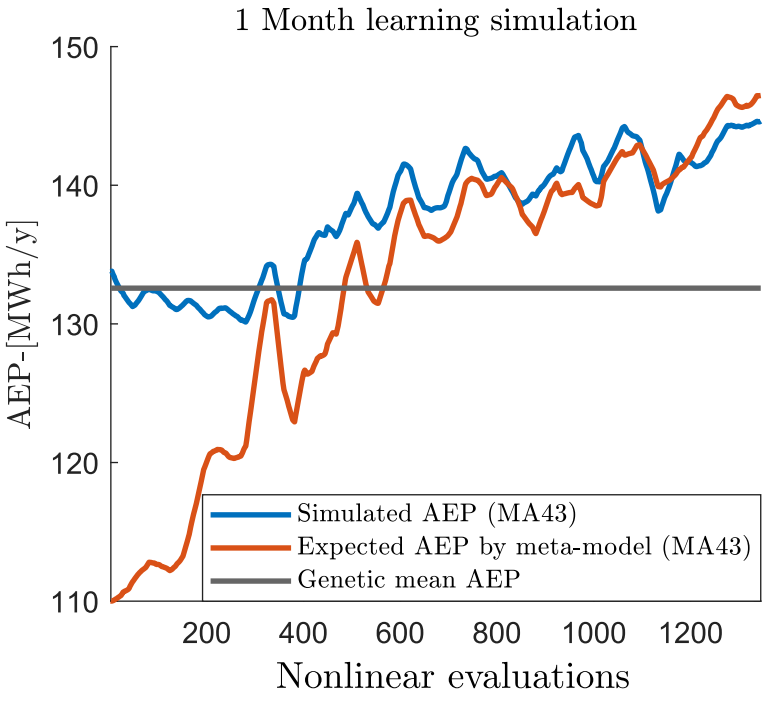

Figure 12: One month simulation results presented with a sliding window of length 43 of the AEP and the e-AEP. The genetic benchmark is represented in grey.

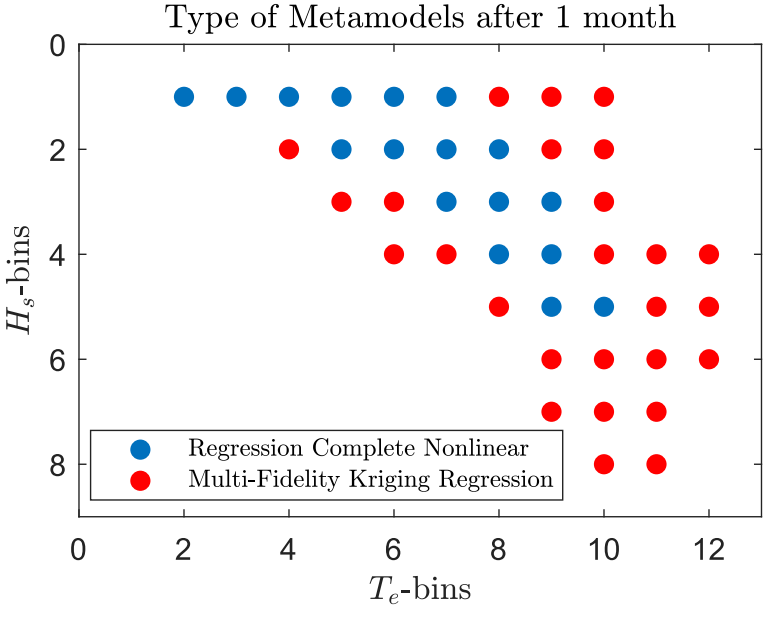

Figure 13: Distribution of the GPR and MF-GPR models after one month of learning.

not enough to totally substitute the previous knowledge. This result suggests that, with additional experiences in those sea-states, the productivity could be further increased.

Some additional remarks may be addressed to the comparison of the presented strategy with respect to other data-driven control applications in wave energy field. First of all, regarding the exploration/exploitation space of the control action, our strategy modifies the parameters that it is trying to optimize in a continous space (each value inside the

boundaries could potentially be applied) similarly to (Anderlini et al., 2017; Pasta et al., 2021d; Parrinello et al., 2020). This constitutes a difference with respect other reinforcement learning strategies applied to the WEC control problem (Anderlini et al., 2016, 2018; Zou et al., 2022). Another difference concerns the control and averaging time steps. The algorithm that we present works with an evaluation every 30 minutes. This may be considered less efficient than other applications like (Zou et al., 2022), where a new control action is performed every 0.1s, or in (Anderlini et al., 2017) where the authors design the control such that changes every 20-40s. Our choice of the time length is motivated by the inverse proportionality between the evaluation time when a reactive control law is applied and the variability that the average power measure has, as well analyzed in Merigaud and Ringwood (2018). For this reason, wanting to reduce the number of evaluations, we designed this evaluation time 30 minutes long. However, this comparison leaves room for possible future improvements to the MF-GPR strategy, where the evaluation time steps are decreased. In the synthesis of the data-driven control strategy, the multi-fidelity approach we introduced, allows the use of data from a model of the system with wrong parameters or even missing some dynamics (here played by the nonlinearities that were approximated in the first-stage linear system). In (Anderlini et al., 2020) a step in this direction with a reinforcement learning strategy is presented, whereas the rest of the data-driven algorithms typically rely on online data.

7. Conclusions and future work

In this work we developed a novel data-driven approach for the optimization of control parameters for a PeWEC device. The main contribution is given by the exploitation of data coming from a previously developed simplified model of the system. This knowledge, affected by the uncertainties characterizing the adopted model, is used to increase the initial learning rate when the target system is deployed. The strategy, based on the creation of a surrogate model following the principles of GPR, requires a limited number of real experiences to adapt prior knowledge based on an inaccurate and simplified model of the system, while also aiming at the maximization of absorbed power. As the simulation results show, the proposed strategy is able to permanently outperform the model-based strategy already after about 400 evaluations. Moreover, the fidelity of the surrogate model increases during the month-long simulation, suggesting further improvement as the learning time is extended. It must be highlighted that developing the MF-GPR approach has a positive impact not only in speeding up the learning process, but also in enhancing the results in the less frequent sea conditions, that are often the most energetic ones. In this way, the adoption of the proposed solution is able to deal with one of the main drawbacks that could characterize learning-based data-driven control in WEC applications: the need of observing a sufficient number of occurrences of wave conditions that are not frequent enough for a pure data-driven approach, but constitute a significant part of the energy that could potentially be extracted. The application of this strategy could be useful in the definition of the control parameters (for the reactive control as done in this work, or for other strategies, like the MPC one) in the initial phase of the deployment, or when an update is necessary due to device aging. Finally, it is worth noticing that the MF-GPR approach is suitable for, but not limited to, an application in which the objective function is purely constituted by the average absorbed power. For this reason, since in this work the direct constraints on the control action are not taken into account, further extensions could be made by adding to the optimization objective, in the form of soft constraints, penalization terms on excessive control efforts or motions, like what has been done by Pasta et al. (2021c) with another data-driven control.

CRediT authorship contribution statement

Daniele Giovanni Gioia: Conceptualization, Methodology, Software, Validation, Formal analysis, Investigation, Data Curation, Writing - Original Draft, Visualization. **Edoardo Pasta:** Conceptualization, Methodology, Software, Validation, Formal analysis, Investigation, Data Curation, Writing - Original Draft, Visualization. **Paolo Brandimarte:** Conceptualization, Resources, Writing - Original Draft, Writing - Review and Editing, Supervision, Project administration. **Giuliana Mattiazzo:** Resources, Writing - Review and Editing, Supervision, Project administration, Funding acquisition.

Fundings

This research has received funding from the Italian National Agency for New Technologies, Energy and Sustainable Economic Development (ENEA), under the project PTR-PTR_19_21_ENEA_PRG_7.

Table 2
Notation Table GPR

GPR Symbols	
i, j	Observations index $1, \dots, n$
y_i and $\mathbf{x}_i$	Observations of the extracted power and corresponding set of control parameter settings with d components each
$\mathcal{D}$	Set of n joint observations
$F(\mathbf{x})$	Metamodel Gaussian function
$m(\mathbf{x})$, μ	Mean function of the Gaussian process and its fixed estimation
$k(\mathbf{x}, \mathbf{x}')$	Array based covariance function of the Gaussian process
$\boldsymbol{\theta}$	Scale parameters of the kernels
$Y(\mathbf{x}), \mathbf{Y}(\mathcal{X})$	Noisy extracted power process (scalar and vector format)
δ	Kronecker delta
ϵ	Gaussian distributed noise with standard deviation λ
$\mathcal{X}$	Control settings into matrix form $\in \mathbb{R}^{d \times n}$
$\mathcal{K}(\mathcal{X}, \mathcal{X})$	Matrix based covariance function of the Gaussian process
l, nl and Δ -subscripts	Quantities related to the *linear* process, the *nonlinear* process and their difference process
$\mathbf{I}_n$	$n \times n$ identity matrix
$\mathbb{S}^n_{++}$	Space of the $n \times n$ symmetric positive definite matrices
f_i	Gaussian process observed values with previously subtracted noise
*-superscript	All the value related to a new observation or prediction
χ	Kernel set iterator
C	Covariance matrix of the multi-fidelity process
$\bar{f}$	Predicted mean according to the Gaussian process
$-i$-superscript	Quantities computed with a reduced sample without the i element of the original pool of observations
$I(\mathbf{x})$	Random variable of the improvement with regards to our actual observed minimum
$p(w, \chi)$	Statistics of the maximum Prediction Error Standardized for each sea state w and kernel χ
s	Estimated standard deviation of the prediction computed with Gaussian hypotheses
$\mathcal{P}(\chi)$	Sets of the maximum values per kernel with regards to all the available sea states w
w	Sea-state index of with non-zero occurrence percentage $Occ_{\%_w} \neq 0$
σ	Variance multiplier of the Gaussian process kernel

Table 3
Notation Table PeWEC

PeWEC Symbols	
t	Time
$X_f(t)$	Vector of the coordinates of the floater motion
$x(t)$ and $z(t)$	Floater surge and heave
$\delta(t)$	Pitch rotation of the floater with respect to the inertial axis y
M	Inertia matrix of both the hull and the internal components of PeWEC
A_∞	Added mass at infinity frequency
K_r	Radiation impulse response functions matrix
K_h	Hydrostatic stiffness matrix
$F_{ext}(t)$	External forces
F_r	Convolution term of the radiation forces acting on the hull
B_v	Coefficients related to the nonlinear viscous forces
A_r, B_r and C_r, and D_r	Radiation state space matrices
$F_{wave}(t)$, $F_{moor}(t)$, $F_{pend}(t)$	Contributions from the wave, the mooring and the reactions that the pendulum and PTO system discharge onto the hull axes
$\eta(t)$	Wave elevation
$S_\eta(\omega)$	Wave spectrum of N superimposed components
ω_n,A_n	Frequency and amplitude of the n-th wave component
θ_n	Random phase of the n-th wave component
$f_{e_{i,n}}$	Excitation force n-th geometry-dependent coefficient, at frequency ω_n computed with respect to the i-th axis
$\mathcal{O}$, $\mathcal{G}$, and $\mathcal{A}$	The global, the floater and the pendulum reference frames
$\varepsilon(t)$	Pendulum oscillation angle with respect to the floater axis y_1
I_y and m	The inertia around the baricentric axis of the pendulum mass and the mass itself
C and K	Damping and stiffness contributions of the reactive control

References

Alevras, P., Brown, I., Yurchenko, D., 2015. Experimental investigation of a rotating parametric pendulum. Nonlinear Dynamics 81, 201–213. doi:10.1007/s11071-015-1982-8.

Anderlini, E., Forehand, D., Bannon, E., Abusara, M., 2017. Reactive control of a wave energy converter using artificial neural networks. International Journal of Marine Energy 19, 207–220. doi:10.1016/j.ijome.2017.08.001.

Anderlini, E., Forehand, D., Bannon, E., Xiao, Q., Abusara, M., 2018. Reactive control of a two-body point absorber using reinforcement learning. Ocean Engineering 148, 650–658. doi:10.1016/j.oceaneng.2017.08.017.

Anderlini, E., Forehand, D.I.M., Stansell, P., Xiao, Q., Abusara, M., 2016. Control of a Point Absorber Using Reinforcement Learning. IEEE Transactions on Sustainable Energy 7, 1681–1690. doi:10.1109/TSTE.2016.2568754.

Anderlini, E., Husain, S., Parker, G.G., Abusara, M., Thomas, G., 2020. Towards Real-Time Reinforcement Learning Control of a Wave Energy Converter. Journal of Marine Science and Engineering 8, 845. doi:10.3390/jmse8110845.

Babarit, A., Delhommeau, G., 2015. Theoretical and numerical aspects of the open source BEM solver NEMOH, in: 11th European Wave and Tidal Energy Conference (EWTEC2015), Nantes, France.

Carapellese, F., Pasta, E., Paduano, B., Faedo, N., Mattiazzo, G., 2022. Intuitive LTI energy-maximising control for multi-degree of freedom wave energy converters: the PeWEC case. Ocean Engineering .

Carapellese, F., Sirigu, S.A., Giorgi, G., Bonfanti, M., Mattiazzo, G., 2021. Multiobjective optimisation approaches applied to a wave energy converter design, in: 14th European Wave and Tidal Energy Conference (EWTEC), Plymouth, UK. pp. 2114–1 – 2114–8.

Erickson, C.B., Ankenman, B.E., Sanchez, S.M., 2018. Comparison of gaussian process modeling software. European Journal of Operational Research 266, 179–192. doi:https://doi.org/10.1016/j.ejor.2017.10.002.

Faedo, N., Carapellese, F., Pasta, E., Mattiazzo, G., 2022. On the principle of impedance-matching for underactuated wave energy harvesting systems. Applied Ocean Research 118, 102958. doi:10.1016/j.apor.2021.102958.

Faedo, N., Dores Piuma, F.J., Giorgi, G., Ringwood, J.V., 2020. Nonlinear model reduction for wave energy systems: a moment-matching-based approach. Nonlinear Dynamics 102, 1215–1237. doi:10.1007/s11071-020-06028-0.

Faedo, N., Olaya, S., Ringwood, J.V., 2017. Optimal control, MPC and MPC-like algorithms for wave energy systems: An overview. IFAC Journal of Systems and Control 1, 37–56. doi:10.1016/j.ifacsc.2017.07.001.

Faedo, N., Peña-Sanchez, Y., Ringwood, J.V., 2018. Finite-order hydrodynamic model determination for wave energy applications using moment-matching. Ocean Engineering 163, 251–263. doi:10.1016/j.oceaneng.2018.05.037.

Faedo, N., Pena-Sanchez, Y., Ringwood, J.V., 2021a. Receding-Horizon Energy-Maximising Optimal Control of Wave Energy Systems Based on Moments. IEEE Transactions on Sustainable Energy 12, 378–386. doi:10.1109/TSTE.2020.3000013.

Faedo, N., Scarciotti, G., Astolfi, A., Ringwood, J.V., 2021b. Nonlinear Energy-Maximizing Optimal Control of Wave Energy Systems: A Moment-Based Approach. IEEE Transactions on Control Systems Technology , 1–15doi:10.1109/tcst.2020.3047229.

Fasshauer, G., 2007. Meshfree Approximation Methods with MATLAB. Interdisciplinary mathematical sciences, World Scientific. URL: https://books.google.it/books?id=gtqBdMEqryEC.

Fontana, M., Casalone, P., Sirigu, S.A., Giorgi, G., Bracco, G., Mattiazzo, G., 2020. Viscous damping identification for a wave energy converter using CFD-URANS simulations. Journal of Marine Science and Engineering 8. doi:10.3390/JMSE8050355.

Forrester, A.I., Keane, A.J., 2009. Recent advances in surrogate-based optimization. Progress in Aerospace Sciences 45, 50–79. doi:10.1016/j.paerosci.2008.11.001.

Forrester, A.I., Sóbester, A., Keane, A.J., 2007. Multi-fidelity optimization via surrogate modelling. Proceedings of the Royal Society A: Mathematical, Physical and Engineering Sciences 463, 3251–3269. doi:10.1098/rspa.2007.1900.

Forrester, A.I.J., Sobester, A., Keane, A.J., 2008. Engineering Design via Surrogate Modelling - A Practical Guide. Wiley.

Garcia-Rosa, P.B., Lizarralde, F., Estefen, S.F., 2012. Optimization of the wave energy absorption in oscillating-body systems using extremum seeking approach, in: 2012 American Control Conference (ACC), pp. 1011–1016. doi:10.1109/ACC.2012.6314858.

Garcia-Violini, D., Pena-Sanchez, Y., Faedo, N., Ringwood, J.V., 2020. An Energy-Maximising Linear Time Invariant Controller (LiTe-Con) for Wave Energy Devices. IEEE Transactions on Sustainable Energy 11, 2713–2721. doi:10.1109/TSTE.2020.2971392.

Garcia-Violini, D., Ringwood, J.V., 2021. Energy maximising robust control for spectral and pseudospectral methods with application to wave energy systems. International Journal of Control 94, 1102–1113. doi:10.1080/00207179.2019.1632491.

Giorgi, G., Davidson, J., Habib, G., Bracco, G., Mattiazzo, G., Kalmár-Nagy, T., 2020. Nonlinear Dynamic and Kinematic Model of a Spar-Buoy: Parametric Resonance and Yaw Numerical Instability. Journal of Marine Science and Engineering 8, 504. doi:10.3390/jmse8070504.

Guo, B., Ringwood, J.V., 2021. Geometric optimisation of wave energy conversion devices: A survey. Applied Energy 297, 117100. doi:10.1016/j.apenergy.2021.117100.

Hals, J., Falnes, J., Moan, T., 2011. Constrained Optimal Control of a Heaving Buoy Wave-Energy Converter. Journal of Offshore Mechanics and Arctic Engineering 133. doi:10.1115/1.4001431.

Jones, D.R., 2001. A taxonomy of global optimization methods based on response surfaces. Journal of Global Optimization 21, 345–383. doi:10.1023/A:1012771025575.

Jones, D.R., Schonlau, M., Welch, W.J., 1998. Efficient global optimization of expensive black-box functions. Journal of Global Optimization 13, 455–492. doi:10.1023/A:1008306431147.

Kennedy, M., O'Hagan, A., 1998. Predicting the output from a complex computer code when fast approximations are available. Biometrika 87. doi:10.1093/biomet/87.1.1.

Kleijnen, J., 2015. Regression and kriging metamodels with their experimental designs in simulation: Review. SSRN Electronic Journal doi:10.2139/ssrn.2627131.

Kleijnen, J., Beers, W., 2019. Statistical tests for cross-validation of kriging models. SSRN Electronic Journal doi:10.2139/ssrn.3395872.

Kleijnen, J.P., 2009. Kriging metamodeling in simulation: A review. European Journal of Operational Research 192, 707–716. doi:https://doi.org/10.1016/j.ejor.2007.10.013.

Krige, D., 1951. A statistical approach to some basic mine valuation problems on the Witwatersrand. Journal of the Southern African Institute of Mining and Metallurgy 52, 119–139. doi:10.10520/AJA0038223X_4792.

Li, G., Belmont, M.R., 2014. Model predictive control of sea wave energy converters – Part I: A convex approach for the case of a single device. Renewable Energy 69, 453–463. doi:10.1016/j.renene.2014.03.070.

Loeppky, J., Sacks, J., Welch, W., 2009. Choosing the sample size of a computer experiment: A practical guide. Technometrics 51, 366–376. doi:10.1198/TECH.2009.08040.

Maria-Arenas, A., Garrido, A.J., Rusu, E., Garrido, I., 2019. Control Strategies Applied to Wave Energy Converters: State of the Art. Energies 12, 3115. doi:10.3390/en12163115.

Mattiazzo, G., 2019. State of the Art and Perspectives of Wave Energy in the Mediterranean Sea: Backstage of ISWEC. Frontiers in Energy Research 7. doi:10.3389/fenrg.2019.00114.

Merigaud, A., Ringwood, J.V., 2018. Free-Surface Time-Series Generation for Wave Energy Applications. IEEE Journal of Oceanic Engineering 43, 19–35. doi:10.1109/JOE.2017.2691199.

Moens de Hase, D., Pasta, E., Faedo, N., Ringwood, J.V., 2021. Towards efficient extremum-seeking control of wave energy systems: possibilities and pitfalls, in: 14th European Wave and Tidal Energy Conference (EWTEC), Plymouth, UK.

Niosi, F., Parrinello, L., Paduano, B., Pasta, E., Carapellese, F., Bracco, G., 2021. On the Influence of Mooring in Wave Energy Converters Productivity: the PeWEC case, in: 2021 International Conference on Electrical, Computer, Communications and Mechatronics Engineering (ICECCME), IEEE, Mauritius. pp. 1–6. doi:10.1109/ICECCME52200.2021.9590867.

Paduano, B., Giorgi, G., Gomes, R.P., Pasta, E., Henriques, J.C., Gato, L.M., Mattiazzo, G., 2020. Experimental validation and comparison of numerical models for the mooring system of a floating wave energy converter. Journal of Marine Science and Engineering 8. doi:10.3390/JMSE8080565.

Paduano, B., Pasta, E., Papini, G., Carapellese, F., Bracco, G., 2021. Mooring Influence on the Productivity of a Pitching Wave Energy Converter, in: OCEANS 2021: San Diego – Porto, IEEE. pp. 1–6. doi:10.23919/OCEANS44145.2021.9706108.

Parrinello, L., Dafnakis, P., Pasta, E., Bracco, G., Naseradinmousavi, P., Mattiazzo, G., Bhalla, A.P.S., 2020. An adaptive and energy-maximizing control optimization of wave energy converters using an extremum-seeking approach. Physics of Fluids 32, 113307. doi:10.1063/5.0028500.

Pasta, E., Carapellese, F., Brandimarte, P., Parrinello, L., Mattiazzo, G., 2021a. A Model-Free Control Strategy Based on Artificial Neural Networks for PeWEC, in: 14th European Wave and Tidal Energy Conference (EWTEC), Plymouth, UK.

Pasta, E., Carapellese, F., Mattiazzo, G., 2021b. Deep Neural Network Trained to Mimic Nonlinear Economic Model Predictive Control: an Application to a Pendulum Wave Energy Converter, in: 2021 IEEE Conference on Control Technology and Applications (CCTA), IEEE, San Diego, US. pp. 295–300. URL: https://ieeexplore.ieee.org/document/9659254/, doi:10.1109/CCTA48906.2021.9659254.

Pasta, E., Faedo, N., Parrinello, L., Carapellese, F., Ringwood, J.V., Mattiazzo, G., 2021c. Constraint handling in extremum-seeking control for wave energy systems: A case study, in: 2021 International Conference on Electrical, Computer, Communications and Mechatronics Engineering (ICECCME), IEEE, Mauritius. pp. 1–6. doi:10.1109/ICECCME52200.2021.9591065.

Pasta, E., Veale, T., Papini, G., Carapellese, F., Bracco, G., Mattiazzo, G., 2021d. Collaborative strategy for model-free control of arrays of wave energy converters: A genetic algorithm approach, in: OCEANS 2021: San Diego – Porto, IEEE, San Diego, CA, USA. pp. 1–7. doi:10.23919/OCEANS44145.2021.9705877.

Pozzi, N., Bonetto, A., Bonfanti, M., Bracco, G., Dafnakis, P., Giorcelli, E., Passione, B., Sirigu, S.A., Mattiazzo, G., 2018a. PEWEC: Preliminary design of a full-scale plant for the Mediterranean Sea, in: Technology and Science for the Ships of the Future - Proceedings of NAV 2018: 19th International Conference on Ship and Maritime Research, pp. 504–514. doi:10.3233/978-1-61499-870-9-504.

Pozzi, N., Bracco, G., Passione, B., Sirigu, S.A., Mattiazzo, G., 2018b. PeWEC: Experimental validation of wave to PTO numerical model. Ocean Engineering 167, 114–129. doi:10.1016/j.oceaneng.2018.08.028.

Pozzi, N., Bracco, G., Passione, B., Sirigu, S.A., Vissio, G., Mattiazzo, G., Sannino, G., 2017. Wave Tank Testing of a Pendulum Wave Energy Converter 1:12 Scale Model. International Journal of Applied Mechanics 9. doi:10.1142/S1758825117500247.

Rasmussen, C.E., Williams, C.K.I., 2005. Gaussian Processes for Machine Learning (Adaptive Computation and Machine Learning). The MIT Press.

Regis, R., Shoemaker, C., 2007. A stochastic radial basis function method for the global optimization of expensive functions. INFORMS Journal on Computing 19, 497–509. doi:10.1287/ijoc.1060.0182.

Ringwood, J.V., 2020. Wave energy control: status and perspectives 2020. IFAC-PapersOnLine 53, 12271–12282. doi:10.1016/j.ifacol.2020.12.1162.

Ringwood, J.V., Bacelli, G., Fusco, F., 2014. Energy-maximizing control of wave-energy converters: The development of control system technology to optimize their operation. IEEE Control Systems 34, 30–55. doi:10.1109/MCS.2014.2333253.

Ringwood, J.V., Mérigaud, A., Faedo, N., Fusco, F., 2020. An Analytical and Numerical Sensitivity and Robustness Analysis of Wave Energy Control Systems. IEEE Transactions on Control Systems Technology 28, 1337–1348. doi:10.1109/TCST.2019.2909719.

Sergiienko, N.Y., Bacelli, G., Coe, R.G., Cazzolato, B.S., 2022. A comparison of efficiency-aware model-predictive control approaches for wave energy devices. Journal of Ocean Engineering and Marine Energy 8, 17–29. doi:10.1007/s40722-021-00214-x.

Sirigu, S.A., Foglietta, L., Giorgi, G., Bonfanti, M., Cervelli, G., Bracco, G., Mattiazzo, G., 2020. Techno-Economic optimisation for a wave energy converter via genetic algorithm. Journal of Marine Science and Engineering 8. doi:10.3390/JMSE8070482.

Stein, M.L., 1999. Interpolation of spatial data. Springer Series in Statistics, Springer-Verlag, New York. doi:10.1007/978-1-4612-1494-6. some theory for Kriging.

Trueworthy, A., DuPont, B., 2020. The Wave Energy Converter Design Process: Methods Applied in Industry and Shortcomings of Current Practices. Journal of Marine Science and Engineering 8, 932. doi:10.3390/jmse8110932.

Yurchenko, D., Alevras, P., 2018. Parametric pendulum based wave energy converter. Mechanical Systems and Signal Processing 99, 504–515. doi:10.1016/j.ymssp.2017.06.026.

Zou, S., Zhou, X., Khan, I., Weaver, W.W., Rahman, S., 2022. Optimization of the electricity generation of a wave energy converter using deep

reinforcement learning. Ocean Engineering 244, 110363. doi:10.1016/j.oceaneng.2021.110363.